中国科学院北京天文台
研究生学位论文

High Resolution Observations With Multi-Channel Solar Telescope

研究生：邓元勇
导师：艾国祥
专业：太阳物理
申请学位：博士
一九九七年二月

北京天文台

中国科学院北京天文台
研究生学位论文

题目 High Resolution Observations With Multi-channel Solar Telescope

研究生 [redacted]
导师 [redacted]
专业 [redacted]
申请学位 博士

一九九七 年 二月

High Resolution Observations with Multi-Channel Solar Telescope

Deng Yuanyong

Beijing Astronomical Observatory
Chinese Academy of Sciences
Beijing 100080, China

Dissertation for the Degree of Doctor of Philosophy

February, 1997

Acknowledgments

I am indebted to my thesis advisor, Professor Ai Guoxiang, member of the Chinese Academy of Sciences, for his constant guidance and encouragement on my work, for countless number of helpful suggestions, and for many kinds of support.

I am grateful to Mr. Song Guofeng, Mr. Wang Jingshan, Mr. Ye Xiangming and Ms. Wang Dongguang for their cooperation during the test observations of the Multi-Channel Solar Telescope (MCST). I would like to thank Mr. Zhang Bin for his continuous cooperation in establishing and developing the high resolution observational system of the MCST.

I express my deepest appreciation to Professors Wang Jingxiu and Zhang Hongqi for many valuable suggestions, discussions and comments.

My special thanks to Professor Li Wei for her unceasing encouragement; to Drs. Wang Huaning, Wang Tongjiang and Liu Yang for their helpful discussions and suggestions; to Professors Ye Binxun and Sun Jinhao for discussions and suggestions on CCD cameras and their accessories; to Professors Qiu Puzhang and Qiu Yaohui, and Mr. Liu Zhong for their cooperation on chapter 5.

I would like to express my appreciation to the Administrator, Li Huanrong, and other staff of Huairou Solar Station for their diligent work to support the observations; to the observers, Ms. Wang Guoping and Mr. Qi Hongwei for their assistance in the observations and experiments.

I am also indebted to the Administrators of Beijing Astronomical Observatory, particularly Ms. Wu Huhong and Ms. Du Hongrong, for many kinds of support.

Finally, special thanks to my wife, Wang Hao, for her continuous encouragement and support.

Preface

The Multi-Channel Solar Telescope (MCST), which is a videomagnetograph and can work at more than nine wavelengths simultaneously, has unique functions in the investigations of the small-scale solar features and 3-dimensional magnetic fields. In the past four years, I have been devoting myself to establishing and developing the high resolution observational system of the MCST. In this thesis, I will summarize the characteristics of the MCST for solar observations and some preliminary results of high resolution observations obtained with this telescope.

This thesis consists of two parts, each of which consists of two themes. In Part I the characteristics of the MCST for solar observations will be introduced. By showing the data obtained during the test observations, I summarize the optical design, operational principle and observational capabilities of the MCST in chapter 2. In chapter 3, I study the inhomogeneous distribution of brightness of a split-element filter used in the MCST. My research indicates that when a birefringent filter with a large field of view is designed, the effect of its integrated transmission must be taken into account in addition to the transmitted profile.

In Part II I report some preliminary results of high resolution observations. I chapter 5, I introduce the application of speckle interference image recovery (SIIR) method in the MCST. The principle of SIIR, the image reception and storage system required by this method will be described in detail. Some recovered images are shown too. In chapter 6, I study the intrinsic properties of magnetic elements in network and plage regions with the magnetic line ratio (MLR) method. This is the first time that the MLR method is used to analyze the real-time magnetograms obtained with a videomagnetograph system. I find that the intrinsic field strengths of magnetic elements trend to decrease from plage, enhanced network to quiet network. In addition, I conclude that there is no obvious correlation between the magnetic filling factors and the intrinsic field strengths.

TABLE OF CONTENTS

PART I

The Multi-Channel Solar Telescope

Chapter 1

Introduction

The history of modern solar observations can date from the 17th century when Galileo firstly observed the Sun with a telescope. From then on, solar physics has made great progress several times with the development of solar instruments. Table 1 summarizes the most important development of solar optical instruments during the past 400 years. In 1814 Fraunhofer found that there are many dark lines in solar spectrum, which were named as Franhofer lines by the later solar physicists. Till today most solar observations depend on this kind of spectral lines. In 1891 Hale invented the spectroheliograph, by means of which he could take the monochromatic image of the Sun over a large field of view by scanning the observed region. Five years later Zeeman discovered that magnetic field can cause the split of spectral lines. Making use of this effect, Hale (1908) measured the strong magnetic fields of sunspots. The birth of Lyot-Ohman birefringent filter in 1930's (Lyot, 1933; Ohman, 1937) made it possible to obtain solar monochromatic image over a large field of view simultaneously. In 1952 Babcock (Babcock, 1953) measured the weak magnetic fields of the Sun with a magnetograph and in 1960 Severny measured solar vector magnetic fields (Severny, 1962). Both Babcock's and Severny's magnetograph can record only one spatial point at a time. A new kind of magnetograph, which can observe 512*1 points at the same time was invented is 1971 (Livingston, 1976). Employing a narrow-band birefringent filter, a videomangnetograph (VMG) can measure solar magnetic fields and line-of-sight velocities over a large field of view at a time. This kind of instruments was invented in the end of 1960's (Beckers 1968; Ramsey 1971) and developed in 1980's (Hagyard *et al.* 1982; Zirin 1985; Ai and Hu 1986). The disadvantage of VMG is that it can work only at one wavelength each time.

From the review cited above and summarized in Table 1 one can see that solar observations have been made significant development in the past 400 years: the observed content has been expanded from taking the white-light and monochromatic image to measuring the polarized light and the spatial dimension from point and line (one-dimension) to area (two-dimension). By this routine the next generation of solar optical instruments should be a system, by which solar polarization over three spatial dimensions can be measured at the same time. However, it is far from easy to realize this kind of instrument. For example, a grating spectrograph requires spatial scanning and a birefringent filter does

spectral scanning in order to measure the polarization (i.e. the magnetic fields) over a wide spectral range (i.e. the dimension parallel to the line-of-sight) and a larger field of view (the other two dimensions orthogonal to the line-of-sight). In a word, a two-dimensional real-time polarizing spectrograph should be an important direction to develop solar instruments.

Table 1. Development of solar optical observations since 17th century*

Observer	Date	Characteristics
Galileo	1611	sunspots, white-light observation
Fraunhofer	1814	dark Fraunhofer lines
Hale	1891	spectroheliograph
Zeeman	1896	Zeeman effect
Hale	1908	strong magnetic field of sunspots, point source
Lyot	1933	monochromatic images over a large field-of-view
Ohman	1938	
Babcock	1952	magnetograph, weak magnetic field, point source
Severny	1960	vector magnetograph, point source
Livingston	1976	magnetograph, line source (512*1 points)
Beckers	1968	magnetograph based on birefringent filter,
Ramsey	1971	two-dimensional source
Ai and Hu	1987	VMG, real-time nine wavelengths

In the past ten years solar physicists have done many experiments in the two-dimensional real-time polarizing spectrograph, one of which is the Multi-Channel Solar Telescope (MCST) (Ai and Hu, 1987a, b and c). Though being a VMG, the MCST can work at more than nine wavelengths simultaneously. This significance makes it especially meaningful for the investigations of the 3-D magnetic fields and small-scale solar structures.

In the following two chapters I will briefly introduce some characteristics of this telescope. In chapter 2, by showing the data obtained during the test observations I describe

*Part of this table is referred to Ai and Hu, 1986

its basic structure, principle and performances for solar observations. In Chapter 3, by analyzing the inhomogeneous distribution of brightness in a split-element filter used in the MCST I indicate that when a birefringent filter with a very large field of view is designed, the effect of its integrated transmission must be taken into account in addition to the transmitted profile.

References

Ai, G., and Hu, Y., 1986, *Acta Astron. Sinica*, **27**, 173

Ai, G., and Hu, Y., 1987a, *Science in China*, p.868

Ai, G., and Hu, Y., 1987b, *Science in China*, p.1969

Ai, G., and Hu, Y., 1987c., *Acta Astrophysica Sinica*, **7**, 305

Babcock, H. W., 1953, *Ap. J.*, **118**, 387

Beckers, J. M., 1968, *Solar Phys.*, **3**, 258

Hagyard, M., Cumings, N., West., E., and Smith, J., 1982, *Solar Phys.*, **80**, 33

Hale, G. E., 1908, *Ap. J.*, **28**, 315

Livingston, W., Harvey, J., Slaughter, C., and Trumbo, D., 1976, *Applied Optics*, **15**, 40

Lyot, B., 1933, *Comptes Rendus*, **197**, 1593

Ohman, Y., 1938, *Nature*, **141**, 157

Ramsey, H. E., 1971, *Solar Phys.*, **21**, 54

Severny, A. B., 1962, *Trans. IAU*, **IIB**, 426

Zirin, H., 1985, *Aust. J. Phys.*, **38**, 961

Chapter 2

Reports on Test Observations with the Multi-Channel Solar Telescope

Accepted by Solar Physics

Abstract.

In this paper, we have made a report on the test observations with a Multi-Channel Solar Telescope (MCST), which consists of 60cm Nine-Channel Solar Telescope (NCST), 35cm Solar Magnetic Field Telescope (SMFT), 8cm Full Disc Telescope (FDT), 10cm Full Disc Magnetic Field Telescope (FDMFT) and 14cm Hα Telescope. These observations demonstrate that the MCST has the following advantages: **a.** It can work at more than nine visible spectral lines simultaneously, in this way, different solar layers of the photosphere and chromosphere can be observed at the same time; **b.** every channel of the NCST is entirely equivalent to a videomagnetograph, by means of which the vector magnetic fields and line of sight velocity fields can be measured; **c.** real-time monochromatic images of the photosphere and chromosphere can be obtained with the FDT, FDMFT and Hα Telescope; **d.** high temporal resolution full-disk magnetic fields can be measured with the FDMFT; **e.** spectral profiles over a large field of view can be scanned with the NCST

1. Introduction

When observing solar magnetic fields, scientists always encounter the following contradiction: large field of view and wide spectral range cannot be obtained simultaneously. For example, a filter system can observe a relatively large area of the solar surface, but it can work only at one wavelength at a time (Mosher, 1976; Title and Rosenberg, 1981; Hagyard *et al.*, 1982; Zirin, 1985; Ai and Hu, 1986a; Lundstedt, *et al.*, 1991); a spectrometer system can observe the Sun over a relatively wide spectral range, but its field of view is quite limited (Livingston *et al.*, 1976; Livingston *et al.* 1976; Micky, 1985; Jones *et al.*, 1992). In order to overcome this contradiction, a new kind of solar instrument, i.e. a two-dimensional real-time spectrometer, which can measure solar magnetic fields over a large field of view and a wide spectral range, is expected.

The Multi-Channel Solar Telescope (MCST) installed at Huairou Solar Station, Beijing Astronomical Observatory, is an experiment in two-dimensional real-time spectrometer (Ai and Hu, 1987a, b, and c). It consists of five parts as shown in Fig. 1: 60cm Nine-Channel Solar Telescope (NCST) (Fig. 1a), 35cm Solar Magnetic Field Telescope (SMFT) (Fig. 1b), 8cm Full Disc Telescope (FDT) (Fig. 1c), 10cm Full Disc Magnetic Field Telescope (FDMFT) (Fig. 1d), and 14cm Hα Telescope (Fig. 1e). In the NCST, a nine-channel birefringent filter splits the incident light into nine polarized exit beams. Thus the MCST can work at thirteen desired spectral lines simultaneously.

The test observations of the whole MCST were finished at the end of 1994. In this paper, we will show some data obtained during these observations. Our purpose is to introduce the capabilities of this telescope to those who are interested in this instrument.

Before our introductions, we would like to note that the MCST is so complicated that it is impossible to introduce all aspects of this system in this report. For example, the SMFT will not be described in detail, since it has been used as a single videomagnetograph (VMG) for more than ten years and is familiar to solar researchers.

2. Nine-Channel Solar Telescope

2.1 Introduction to the telescope and its filter

The NCST was put into use in 1994. It is a vacuum Gregorian system. Its aperture is 60cm and the focal length can be adjusted to 12m, 6m and maybe 4m in the future. The signals from the telescope are collected by CCD cameras. MINTRON MTV-1802 CCDs were used in the test observations. The minimal detectable illumination of this kind of CCD is 0.02Lux, the signal-to-noise ratio is 48dB, and the effective exposure time is 20ms per frame. After 8-bit A/D conversion, the signals collected by the CCD cameras are converted into digital data and stored in optical discs or magnetic tapes. In the case of 6m focal length,

the overall resolution of the NCST is about 0."54×0."38/pixel and the field of view is 4.'5× 3.'2.

The core part of the NCST is a wide-field universal nine-channel birefringent filter schematically shown in Fig. 2(a). In this figure, PBs denote polarizing beam splitters and ARs total reflection prisms. The other optical elements, such as polaroids, birefringent crystals and achromatic waveplates are not shown. From Fig. 2(a), one can see that nine different solar layers can be observed at the same time.

The overwhelming advantage of the nine-channel filter is that each channel is entirely equivalent to a universal birefringent filter. This unique capability is achieved by means of the polarizing beam splitters. The role of the polarizing beam splitter is shown in Fig. 2(b). In a typical filter unit (Lyot element, Evans element or Solc element), the incident linear polarized light can be represented by two components after it passes through the birefringent crystal. The transmissions of these two components are

$$\tau_{//} = \cos^2 n\pi,$$

and

$$\tau_{\perp} = \sin^2 n\pi$$

in the direction parallel and orthogonal to the polarized direction of the incident light, respectively. Here, n denotes the retardation of the birefringent crystal. Then, when the light meets the second polaroid ($\mathbf{P}_2$), the parallel component ($\tau_{//}$) will pass through and the orthogonal component be blocked. In the nine-channel filter, the second polaroid is replaced by a polarizing beam splitter. In this case, the orthogonal component is no longer blocked. It will emerge from the direction vertical to the direction of the incident light. Hence, using m polarizing beam splitters, we can obtain m+1 exit polarized beams (*i.e.* m+1 channels) and do not lose any useful light as compared with a typical filter. In Fig. 2, the total reflection prisms are used to maintain the exit lights parallel.

Some parameters of the nine-channel filter are listed in Table 1. In this table, IDENT means line identification, T is the overall transmission (including KD*P modulator), and N is the number of the basic filter elements used in each channel. The value of the sidelobe is the ratio of the integrated sidelobe to the integrated mainband. The ninth elements of the

channels of FeI5250.212, FeI5247.061 and MgI 5172.699 are Solc elements. Excepting them, all the filter units are Lyot elements.

The nine-channel filter is operated at 42±0.01°C. The wavelength shift caused by ± 0.01°C temperature fluctuation is about ±0.002Å for the channels of FeI5250.211 and FeI5247.061.

Table 1 Some Parameters of the Nine-Channel Birefringent Filter

λ(Å)	IDENT	FWHM(Å)	T(%)	Sidelobe(%)	N
3968.470	Ca II (H)	2.424	20.0	10.72	5
4685.682	He II	0.462	12.0	10.74	8
5172.699	Mg I	0.092	6.0	10.75	10
5247.061	Fe I	0.048	3.0	10.74	11
5250.212	Fe I	0.048	3.0	10.74	11
5576.097	Fe I	0.057	5.0	10.74	11
5875.743	He I (D_3)	0.079	5.5	10.74	11
6302.507	Fe I	0.092	6.0	10.74	11
6562.808	Ha	0.106	7.0	10.74	11

In the following subsections, we will introduce some capabilities of the NCST.

2.2 White light and monochromatic images

Image quality is one of the most important parameters to represent the performances of a telescope. In this subsection, we will give two examples to show the image quality of the NCST.

Figure 3 is a white light image of granulation located at the disc center. There is a sunspot near the upper left of this region. This image was obtained on Jun. 04, 1993. When we took it, the nine-channel filter was replaced by an interference filter whose passband was

5250±50Å. The resolution of the reception system was about 0".089×0".063/pixel and the exposure time of the CCD camera was 1ms. The field of view of this picture is about 30"× 17". One can see that the dimension of the smallest resolvable structures is not larger than 0".4.

Figure 4 is a Hα monochromatic image obtained on Sep. 27, 1994. The field of view is about 4'.5×3'.2, and the exposure time of the CCD camera is 20ms. The fine structures of Hα are quite clear in this figure.

2.3 Magnetograms

The most important capability of a VMG is to get the information of the magnetic fields. We have reported the first measurement of solar magnetic fields with the NCST (Deng *et al.*, 1994). In this subsection, we will show two groups of magnetograms, one of which describes the characteristics of the NCST as a universal filter system, and the other represents its capability to observe the Sun over a large field of view and a wide spectral range simultaneously.

Normally, 255 images are integrated in order to improve the signal-to-noise ratio of a magnetogram. In this observational mode, the minimal detectable strength of the longitudinal magnetic fields is 4.2 Gauss for the spectral line of FeI5250.211. This magnetic sensitivity is similar to that of the MSFC Vector Magnetograph using the same spectral line (Hagyard *et al.*, 1982).

A simple method has been used to calibrate the magnetograms shown in this paper. We will summarize this calibration method in this paragraph. For the longitudinal magnetic fields,

$$I_{L(\lambda)} = I_{R(\lambda)} = \frac{1}{2} I_{(\lambda)},$$

where, $I_{(\lambda)}$ is the line profile and L and R represent the left and right circular polarized light, respectively. The signals of the left and right circular polarized light recorded by the CCD cameras (S_L and S_R,) are

$$S_{L,R} = \int F_{(\lambda)} I_{L,R} d\lambda$$

and the magnetic signal (S) is

$$S = {}^{(S_L - S_R)}\!/\!_{(S_L + S_R)}.$$

Here, $F_{(\lambda)}$ is the profile of the filter and can be calculated from the design parameters. Hence, knowing the line profile $I_{(\lambda)}$, we can determine the calibration coefficient of the longitudinal magnetic fields. In the present work, we have made use of the line profiles provided by Livingston. A similar method can be used to calibrate the transverse fields.

Because the nine-channel filter is a wide-field universal filter, each channel can be tuned to the other spectral lines besides its design wavelength. Fig. 5 gives such an example. In this figure, the longitudinal magnetograms of FeI5247.061, MgI5172.699 and FeI5250.211 (Fig. 5(b), (c) and (d)) were obtained with the channel whose design wavelength is MgI5172.699. Fig. 5(a) is a magnetogram of FeI5324.19 obtained with the SMFT. Because our calibration method is not very exact, because these four Fraunhofer lines are formed in three different solar layers, and because these four magnetograms were not obtained at the same time, we can conclude only that the morphologies of these magnetograms are similar.

Figure 6 is an example of the real-time measurements performed at FeI5247.061 and FeI5250.211. In this figure, we can also see that the morphologies of the measured magnetic fields are similar. Although we have shown only the real-time magnetograms of two channels, we can use more channels to observe the Sun at the same time. These real-time data are very meaningful for solar research, especially for the investigation of the 3D magnetic structures and small-scale magnetic fields.

2.4 Spectral profile

Generally, a filter system is not used to scan the spectral profiles because it works only at a narrow waveband at a time. However, if the filter is a universal filter, it can scan the spectral profiles when its passband is tuned step by step from one wing of a spectral line to the other wing. In this mode, the filter system has obvious disadvantages in comparison

with the spectrometer system: relatively lower spectral and temporal resolution, and unsimultaneous spectral information. Even so, this observational mode is useful in some cases because of its larger field of view.

The NCST can scan solar spectral profiles because its nine-channel birefringent filter is a universal filter. When it works in this mode, the spectral resolution is determined by the FWHM of the filter and the scan interval; the time resolution is limited by the time spent in adjusting the passband, which is tuned by ratable half waveplates driven by step motors.

Figure 7 shows a spectral profile of MgI 5172.699 scanned with the NCST. The solid line is the observed curve, in which the dark current and straylight have been corrected. The object is a quiet region located at the disc center. The sample number is 54 and the sample interval about 0.036Å. It took about twelve minutes to obtain this profile. In order to remove the effects of the small-scale structures, the observed region was smoothed by 3."6× 2."6 (Naturally, this process is not necessary in actual astronomical observations). The dashed line is the convolution of the profiles of the spectral line and the filter. The spectral profile whose resolution is 0.003467Å was provided by Livingston.

From these two curves, we can estimate the additional straylight produced by the incomplete optical elements and inadequate adjustment. With the data from -0.108Å to +0.108Å of the line center, we deduced that the average straylight is about 19%. This value is slightly larger than the straylight of the SMFT (about 17%, Ai and Hu, 1986b).

The correlation coefficient between the two curves of Fig. 7 is about 0.95. We think that the error of the measurement was mainly caused by two factors. Firstly, the spectral resolution of the NCST is much lower than the resolution of Livingston's data. Secondly, although the accuracy of a single step-motor is higher than $FWHM/150$, serious mismatch will probably occur because ten step-motors were used in the channel of MgI5172.699. Now we are carrying out some experiments in improving the accuracy of the step-motors and increasing the scan speed. For example, we intend to replace the step-motors with some instruments driven by electromagnetic effects. In this way, we hope that the time resolution can be increased at least five times.

In the above we have given only the example of scanning the non-polarized spectral profile. The other kinds of profiles, for example the profiles of Stokes' parameters, can be obtained by the same method.

2.5 Line-of-sight velocity

If not considering the change of the observed object during the observation, we can deduce the line-of-sight velocity from the spectral profile. In order to check this capability, we measured the solar rotational velocity with the channel of Fe5247.061. The results are shown in Fig. 8. The sample interval is about 0.01Å which corresponds to a Doppler shift of 0.57km/s at the wavelength of Fe5247.061. We observed both the east and west limb at the solar equator in order to increase the precision. In this case, the measuring accuracy is ± 0.0025Å or ±0.14km/s. At each limb, the sample number is 25 which took about eight minutes. From Fig. 8 we deduce that the solar rotational velocity is about 2.0±0.14km/s at the equator.

3. 8cm Full Disc Telescope

The FDT was put into operation in 1991. It uses a Day-star filter whose design wavelength is CaII3933.664 (CaII K) and FWHM 2Å. The full-disk solar activities can be monitored with this telescope. Fig. 9 is an example obtained on Oct. 04, 1991.

4. 10cm Full Disc Magnetic Field Telescope

The FDMFT is a VMG and was put into operation in 1991. Its birefringent filter whose FWHM is about 0.1Å can work at two spectral lines, one is FeI5324.185 for the measurement of the full-disk vector magnetic fields, the other is FeI5576.097 for the measurement of the full-disk line-of-sight velocities. The spatial resolution of the reception

system is about 4."0/pixel. The minimal detectable strength of the longitudinal magnetic fields is about 4G and that of the transverse magnetic fields about 60G in case of integrating 255 images, which requires 40s observational time. Compared with the Kitt Peak full disc magnetograph (Jones *et al.*, 1992), our system has higher temporal resolution, similar sensitivity, and lower spatial resolution. Fig. 10 shows a full-disk longitudinal magnetogram obtained on Oct. 04, 1991.

5. 14cm Hα Telescope

The 14cm Hα Telescope was put into operation in 1991. It is used to observe the activities of the solar chromosphere. The passband of its birefringent filter is 0.5Å and can be adjusted ±32Å from the line center, so white light flares can be observed with this telescope. The full disc and a medium-size field of view can be observed simultaneously. The medium-size field of view is 12'.8×8'.0. Usually, the data is recorded by videocorder, but it can be stored digitally too. Fig. 11 is an image of an active region obtained on May 15, 1995.

6. Summary and Further Developments

Based on the above introductions, the advantages of the MCST can be summarized as follows: a. it can work at more than nine visible spectral lines simultaneously, in this way, different solar layers of the photosphere and chromosphere can be observed at the same time; b. every channel of the NCST is entirely equivalent to a videomagnetograph, by means of which, the vector magnetic fields and line of sight velocity fields can be measured; c. real-time monochromatic images of the photosphere and chromosphere can be obtained with the FDT, FDMFT and Hα Telescope; d. high temporal resolution full-disk magnetograms can be measured with the FDMFT; e. spectral profiles over a large field of view can be scanned

by tuning the passband of the nine-channel birefringent filter step by step from one wing of a spectral line to the other wing.

At the end of this article, we would like to introduce some plans to improve the MCST. Firstly, as mentioned in Subsection 2.4, we intend to replaced the step-motors with some new kinds of motors in order to tune the passband of the filter faster and more accurately. Secondly, we plan to develop the reception system, especially, the CCD cameras. The MINTRON MTV 1802 CCD currently used in our system, is a kind of commercial CCD. Its function does not match with that of the MCST though it is quite cheap. We have been testing several kinds of CCDs, such as PULNIX (America) and DALSA (Canada) CCDs. Finally and most importantly, we should develop some softwares and techniques to analyze the observational data of the MCST.

Acknowledgment

The MCST was manufactured by Nanjing Astronomical Instrument Factory(NAIF). We are indebted to all people of NAIF for their contribution to this instrument. Thanks are also due to Prof. Livingston for providing the spectral profiles and Dr. Wang Huaning for his discussions. The MCST program was supported by the Chinese Academy of Sciences and the National Natural Science Foundation of China.

Reference

Ai, G., and Hu, Y., 1986a, *Acta Astron. Sinica*, **27**, 173

Ai, G., and Hu, Y., 1986b, *Publications of the Beijing Astronomical Observatory*, **6**, 111

Ai, G., and Hu, Y., 1987a, *Science in China*, p.868

Ai, G., and Hu, Y., 1987b, *Science in China*, p.1969

Ai, G., and Hu, Y., 1987c., *Acta Astrophysica Sinica*, **7**, 305

Deng Y., Ai, G., Wang, J., *et al.*, 1995, In: *proceeding of the third China-Japan seminar on solar physics*, Wang *et al.* (*eds.*), International Academic Publishers, 298

Hagyard, M., Cumings, N., West., E., and Smith, J., 1982, *Solar Phys.*, **80**, 33

Jones, H., Duvall, T., Harvey, J., *et al.*, 1992, *Solar Phys.*, **139**, 211

Mosher, J. M., 1976, *BBSO reprint,* No. **0159**

Livingston, W., Harvey, J., Pierce, A., *et al.*, 1976, *Applied Optics*, **15**, 33

Livingston, W., Harvey, J., Slaughter, C., and Trumbo, D., 1976, *Applied Optics*, **15**, 40

Lundstedt, H., Johannesson, A., *et al.*, 1991, *Solar Phys.*, **132**, 233

Micky, D., 1985, *Solar Phys.*, **97**, 223

Title, A., and Rosenberg, W., 1981, in *Proc. Sac. Peak Nat. Obs. Conf.*, Dunn (*eds.*), Sunspot, NM: Sac. Peak Obs., p. 326

Zirin, H., 1985, *Aust. J. Phys.*, **38**, 961

Captions

Fig. 1 Sketch of the Multi-Channel Solar Telescope

BF: birefringent filter **UBF**: universal **BF**

KD*P: KD*P modulator **IF**: interference filter

(a). **60cm Nine-Channel Solar Telescope (NCST).** It can work at nine wavelengths simultaneously. The vector magnetic fields and line-of-sight velocities of the photosphere and chromosphere can be measured with this telescope.

(b). **35cm Solar Magnetic Field Telescope (SMFT)**. Two wavelengths can be selected alternatively, one is FeI5324.185 that is formed in the photosphere, the other is Hβ that is formed in the chromosphere. The vector magnetic fields and line-of-sight velocities can be measured with this telescope.

(c). **8cm Full Disc Solar Telescope.** It works at CaII3933.664. The FWHM of its Day-star filter is 2Å.

(d). **10cm Full Disc Magnetic Field Telescope.** Two wavelengths can be selected alternatively. FeI5324.185 is used to measure the full-disk vector magnetic fields and FeI5576.097 to measure the full-disk line-of-sight velocities of the photosphere.

(e). **14cm Hα Telescope.** The full disc and a medium-size field of view of the Sun can be observed simultaneously with this telescope. The passband of its filter can be adjusted ±32Å from the Hα line center.

Fig. 2 The nine-channel birefringent filter and its principle

(a). Sketch of the nine-channel birefringent filter

(b). The principle of the nine-channel birefringent filter

PB: polarizing beam splitter **AR:** total reflection prism.

BC: birefringent crystal P_1, P_2: polaroid

The other optical elements, such as birefringent crystals, polaroids and achromatic waveplates, etc., are not shown in this figure. When the light passes through a PB, it is split into two emergent beams by their polarized directions. The role of ARs is to maintain the exit lights parallel.

Fig. 3 White light image of granulation obtained with the NCST

The observed region was at the disc center, and a sunspot located near the upper left of this panel. When this image was got, the nine-channel birefringent filter was replaced by an interference filter whose passband is 5250±50Å. The field of view is about 30"×17" and the exposure time is 1ms. The smallest resolvable structures are not larger than 0".4.

Fig. 4 Monochromatic image of Hα obtained with the NCST

The field of view is 4.'5×3.'2 and exposure time 20ms. The active region is near the solar limb.

Fig. 5 Magnetograms of an active region obtained at different spectral lines

(b), (c), and (d): magnetograms of FeI5247.061, MgI5172.699 and FeI5250.211 obtained with the channel of the NCST whose design wavelength is MgI5172.699.

(a). magnetogram of FeI5324.185 obtained with the SMFT on the same day.

Although these four spectral lines are formed in different layers of the Sun, one can see that the morphologies of the magnetic fields are similar.

Fig. 6 An example of the real-time measurements of solar magnetic fields with the NCST

Fig. 7 Spectral profile of MgI5172.699 scanned by the NCST

The solid line is the observed data in which the straylight and dark current have been corrected. The sample interval is 0.036Å. The dashed line is the convolution of the spectral profile provided by Livingston and the profile of the filter calculated from the design parameters. The spectral resolution of Livingston's data is 0.003467Å. Circles denote sample points. The correlation coefficient between these two curves is about 0.95.

Fig. 8 Solar rotational velocity measured with the NCST

The used spectral line is FeI5247.061 and the sample interval is 0.01Å that corresponds to a Doppler shift of 0.57km/s at this wavelength. The solid and dashed lines are the spectral profiles obtained at the west and east limbs at the solar equator, respectively. From these two curves, we deduce a solar rotational velocity at the equator of about 2.0±0.14km/s.

Fig. 9 Full-disk monochromatic image of CaII3933.664 obtained with the FDT

Fig. 10 Full-disk longitudinal magnetogram of FeI5324.185 obtained with the FDMFT

Fig. 11 Monochromatic image obtained with the 14cm Hα telescope

The field of view is 12'.8×8'.0. There is a flare near the image center.

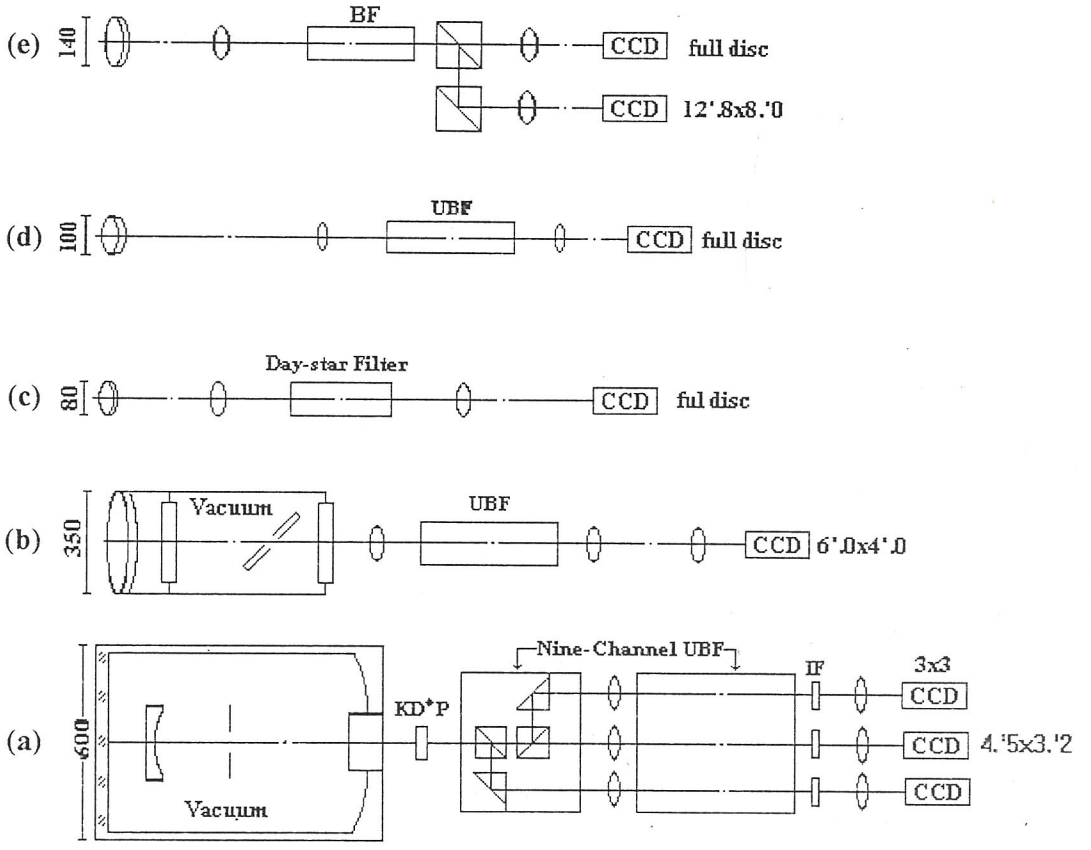

Figure 1. Sketch of the Multi-Channel Solar Telescope

BF:	birefringent filter	UBF:	universal BF
KD*P:	KD*P modulator	IF:	interference filter

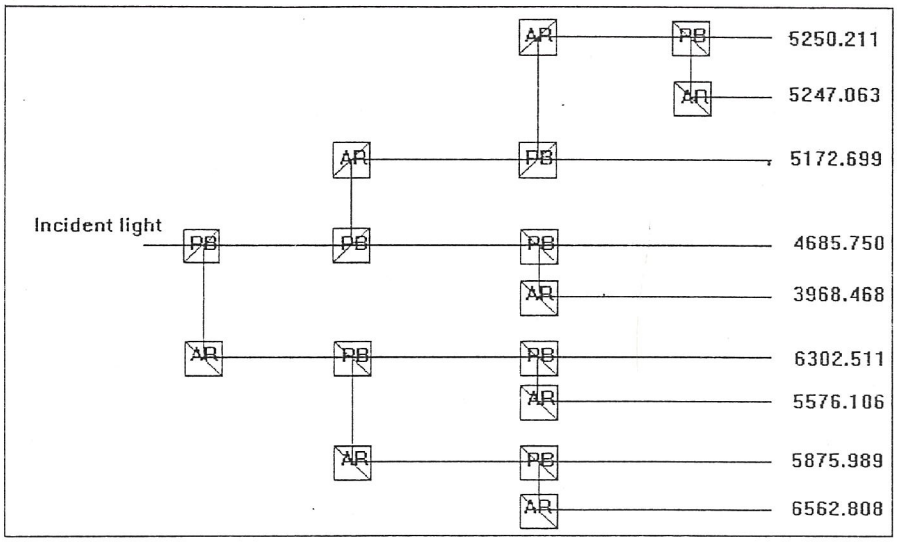

(a). Sketch of the Nine-Channel Birefringent Filter

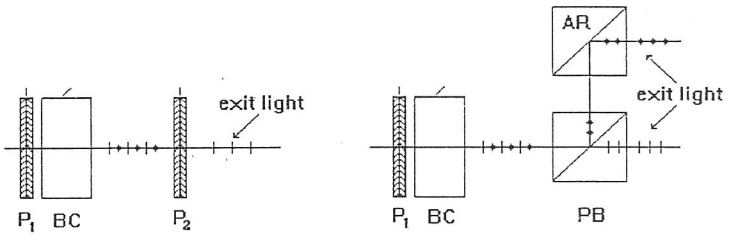

a typical Lyot element　　a modified Lyot element

(b). Principle of the Nine-Channel Birefringent Filter

Figure 2. Nine-Channel Birefringent Filter and its principle

PB: polarizing beam splitter　　AR: total reflection prism

BC: birefringent crystal　　P_1, P_2: polaroid

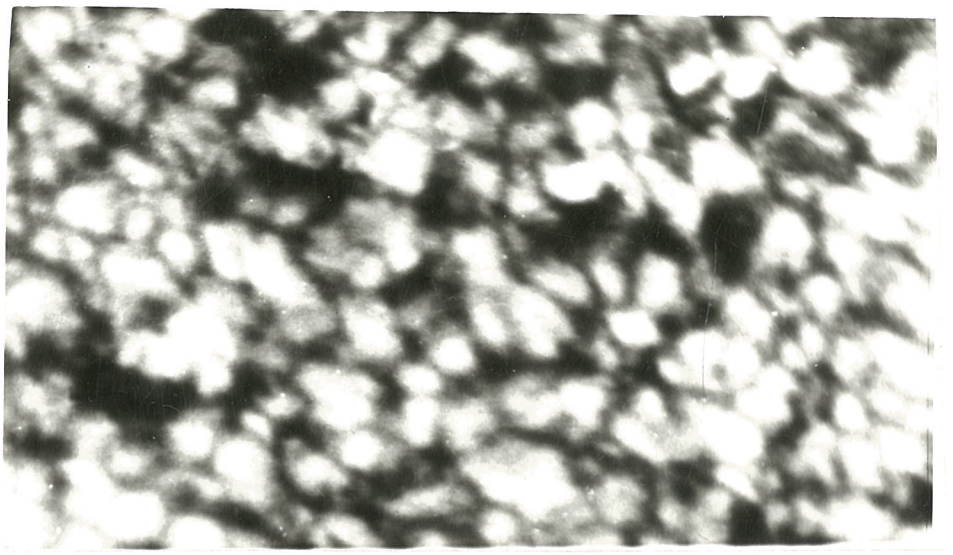

Figure 3. White light image of granulation obtained with the NCST

Figure 4. Monochromatic image of Hα obtained with the NCST

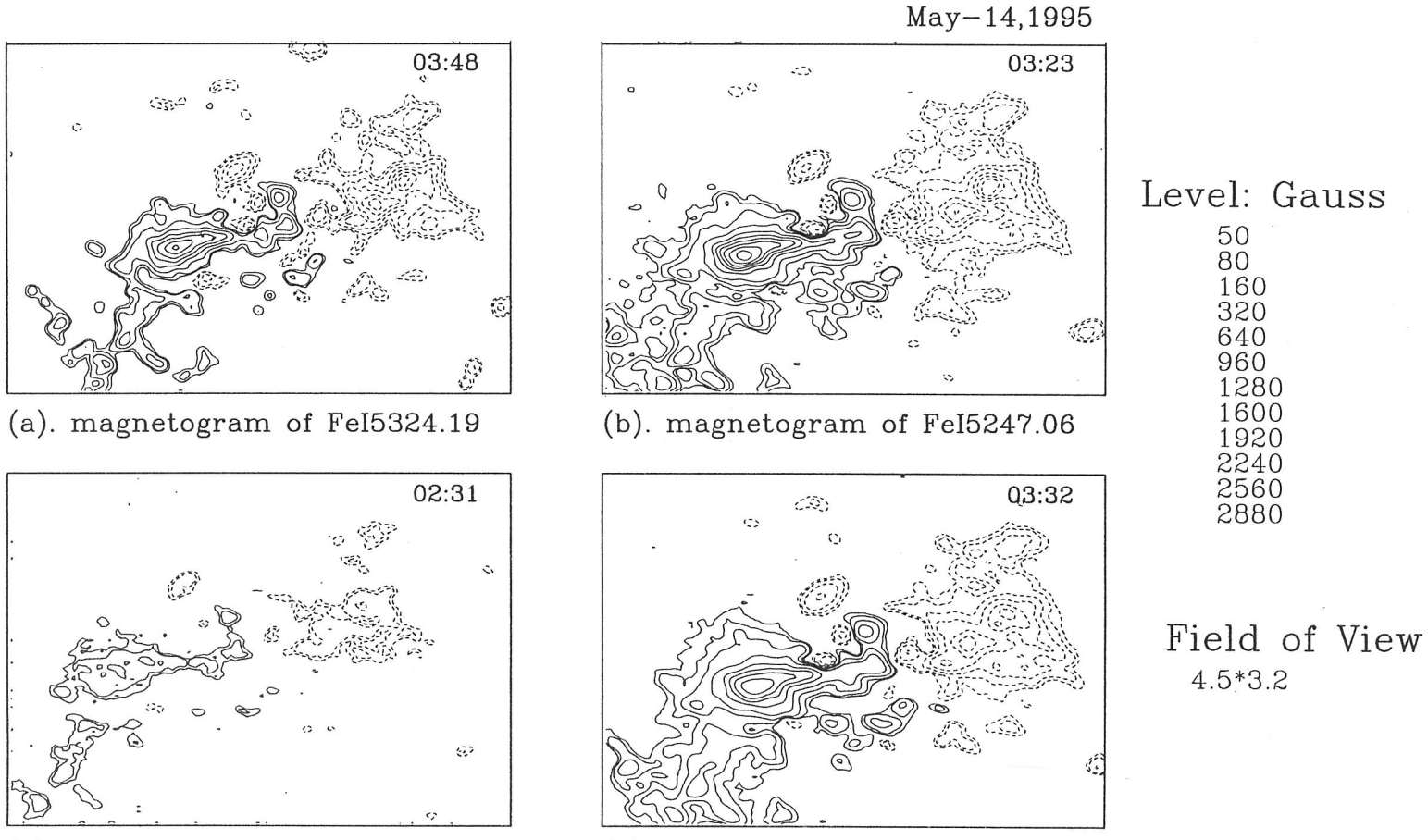

(a). magnetogram of FeI5324.19

(b). magnetogram of FeI5247.06

(c). magnetogram of MgI5172.699

(d). magnetogram of FeI5250.22

Figure 5 Magnetograms obtained in different lines by one channel

(b).(c).(d): magnetograms obtained by the channel whose designed passband is MgI5173

(a) magnetogram obtained by SMFT on the same day

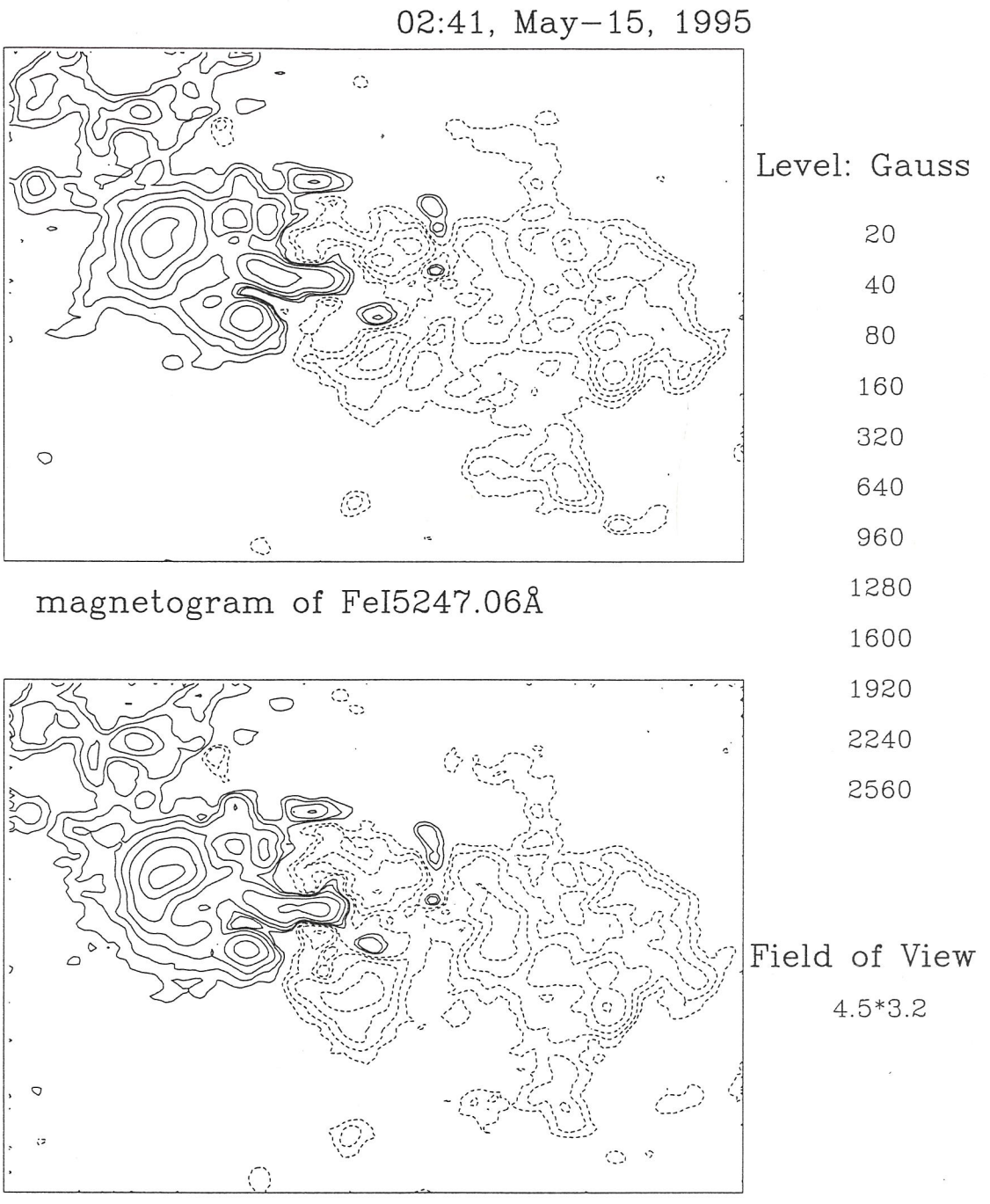

Figure 6 Example of real-time magnetograms

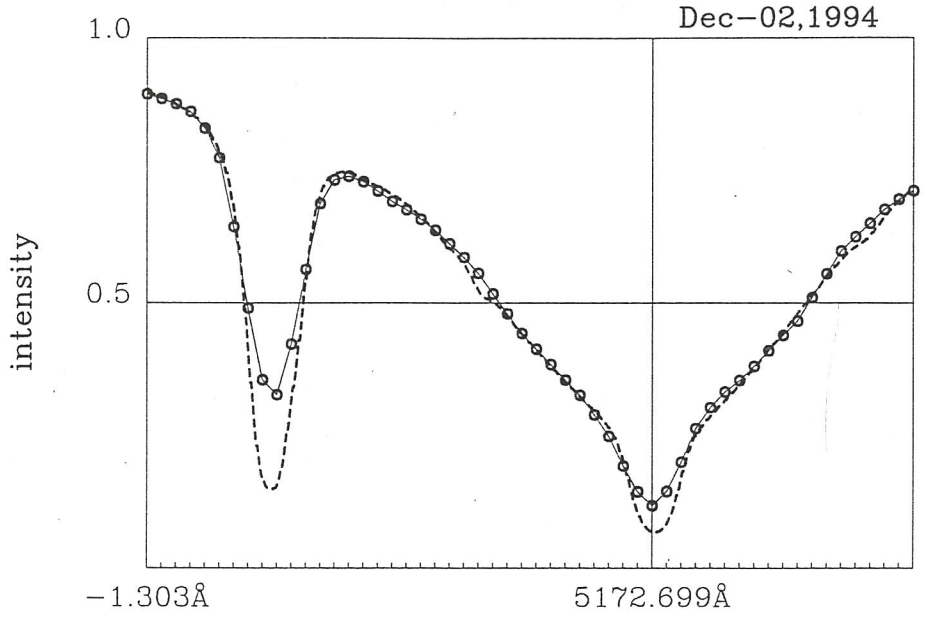

Figure 7. Spectral profile of MgI5172.699Å

Solid line : observed profile
Dash line : Livingston's data
circle: sample point

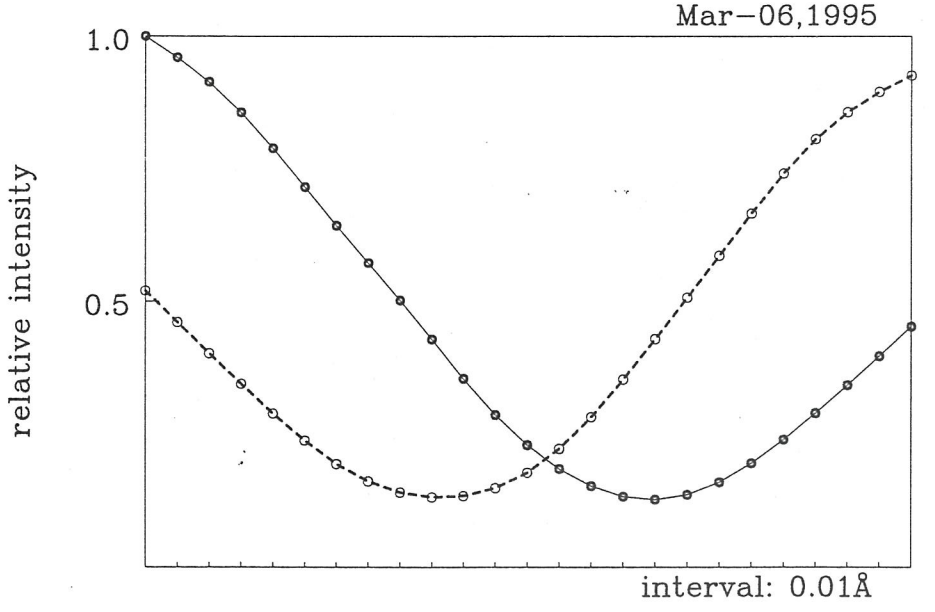

Figure 8. Solar rotation measurement with NCST

solid line: spectral profile of west edge
dash line: spectral profile of east edge
circle: sample point

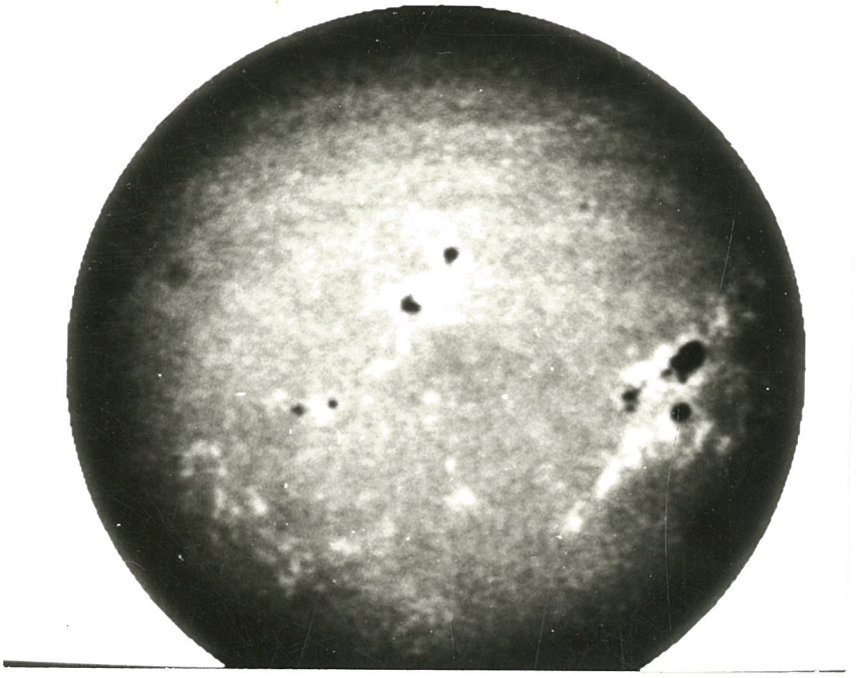

Figure 9. Full-disk monochromatic image of CaII3933.664 obtained with the FDT

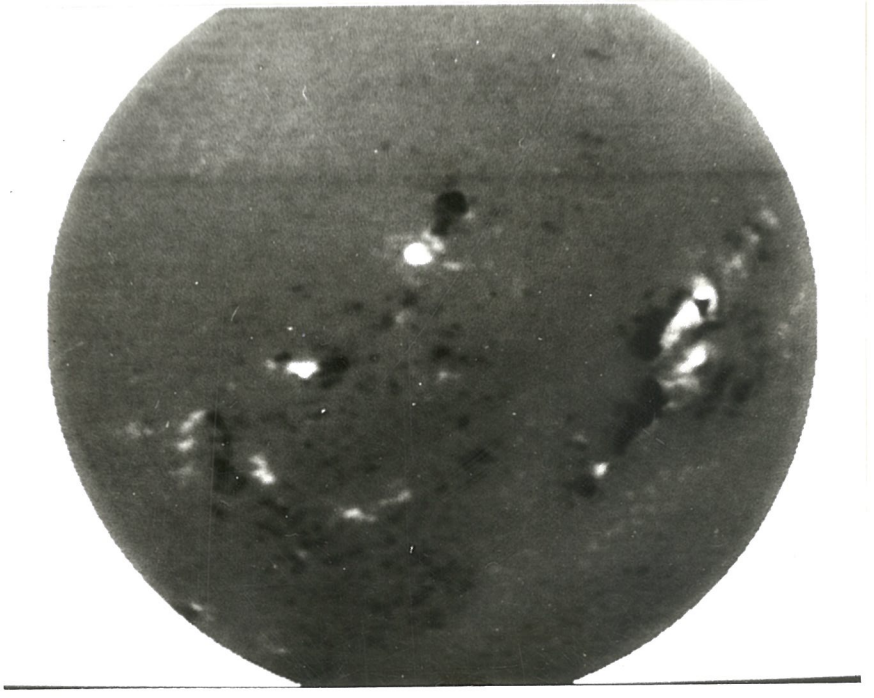

Figure 10. Full-disk longitudinal magnetogram of FeI5324.185 obtained with the FDMFT

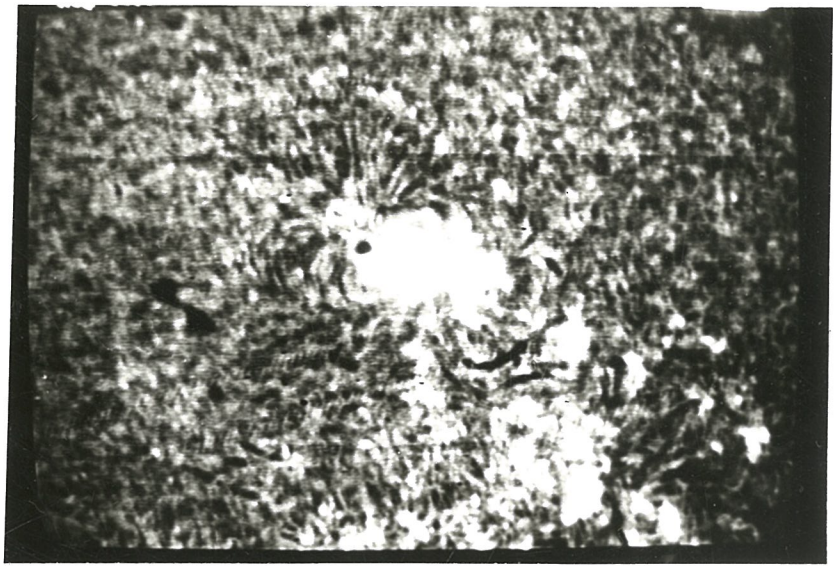

Figure 11. Monochromatic image obtained with the 14cm Hα telescope

Chapter 3

Inhomogeneous Distribution of Brightness in Split-Element Filter

Applied Optics, 1997, Vol. 36, No. 7, 1

Abstract

The inhomogeneous distribution of brightness in split-element filter is discussed in this paper. This inhomogeneity is caused by the off-axis effect of birefringent crystal and can seriously affect astronomical observations in case of large field of view. For example, the maximal brightness fluctuation is about 9.44% in a full disc solar telescope whose maximal incident angle is 70'. We also discuss the ways to avoid this disadvantage.

1. Introduction

The design scheme of split-element filter[1] was proposed firstly by J. Evans in 1949. According to this scheme, one split-element unit is equivalent to two Lyot's elements, but saves one polaroid. This improvement is very meaningful because the transmission of polaroid is very lower than that of other optical elements used in birefringent filter.

On the other hand, this design has some disadvantages. For example, its inhomogeneity of brightness distribution caused by the off-axis effect is the most serious one. Evans thought that one unit of split-element filter is equivalent to such Lyot's filter, which consists of one thinner simple element and one thicker wide-field element, *i.e.*, split-element filter has wide field characteristics. In fact, this view is not proper. Evans himself had also found this misunderstanding[2]. In 1979, A. M. Title and W. J. Rosenberg had given detailed knowledge of the off-axis effect[3]. These results had clearly revealed how the off-axis effect affects the transmitted profile of birefringent filter. Unfortunately, none of these authors had discussed the following questions in detail: How does the off-axis effect affect the integrated transmission of split-element filter? How serious is this effect for astronomical observations?

In this paper, we can see that the brightness distribution of split-element filter is inhomogeneous because its integrated transmission is not constant. This effect is especially serious when the field of view is large. For example, the maximal brightness difference is

about 9.44% in the Full Disc Solar Magnetic Field Telescope used in Huairou Solar Station, Beijing Astronomical Observatory. Our discussions begin with the basic structure (Subsection 2.1) and equations (Subsection 2.2) of split-element filter. In Subsection 2.3 we analyses the inhomogeneity of brightness distribution qualitatively, and in Subsection 2.4 we analyses it quantitatively. The effects of this inhomogeneity for astronomical observations are sampled in Subsection 2.5. At the end of this paper, we emphasize that in optical region it is unsuitable to use split-element filter because the transmission of polaroid is very high, while in UV, infrared and other wavebands, split-element filter still has its superiority over Lyot's filter.

2. The inhomogeneity of brightness distribution in split-element filter

2.1 Structure of split-element filter

The basic structure of split-element filter is shown in Fig.1a. The components ***m*** and ***q*** are named as split element, and ***p*** is middle element that is sandwiched between ***m*** and ***q***. $\mathbf{P}_1$ and $\mathbf{P}_2$ are polarizers. n_{m}, n_{q} and n_{p} denote the retardations of these components, respectively. Then the transmission of this unit is

$$\tau = \sin^2 \pi(n_m - n_q) + \sin 2\pi n_m \sin 2\pi n_q \sin^2 \pi n_p \qquad (1)$$

The design of split-element filter requests:

$$n_j = 2n_m = 2n_q = 2^{j-1} n + \frac{1}{2}, \qquad (2)$$

$$n_p = 2^{k-1} n + \frac{1}{2}, \qquad (3)$$

where ***n*** is an integer, ***j*** and ***k*** correspond to the classes of the split element and middle element in the filter. In this case, Equation 1 can be substituted by

$$\tau = \sin^2 \pi n_p \sin^2 \pi n_j \qquad (4)$$

Thus, one split-element unit is equivalent to two Lyot's elements shown in Fig.1b.

2.2 The off-axis effect in split-element filter

Unfortunately, Equation 4 can hardly be satisfied exactly because of the off-axis effect and the errors caused by manufacture. The effects resulting from these errors will affect the transmitted profile of birefringent filter as we have mentioned in the introduction. Furthermore, they will affect the integrated transmission. In the following, one can see that this effect is more serious in split-element filter than in Lyot's filter. Here we only discuss the effect caused by the off-axis effect. In order to simplify our following discussion, we assume that the filter is formed by one split-element unit whose middle element is wide-field, and

$$n_j = n + \frac{1}{2}, \tag{5}$$

$$n_p = 2n + \frac{1}{2}. \tag{6}$$

If the incident light traverses this filter at angle (φ,θ) to the instrumental axis, then

$$n_m = \frac{n_j}{2}[1 + \varphi^2\kappa(\frac{\cos^2\theta}{\gamma} - \frac{\sin^2\theta}{\alpha})], \tag{7}$$

$$n_q = \frac{n_j}{2}[1 + \varphi^2\kappa(\frac{\sin^2\theta}{\gamma} - \frac{\cos^2\theta}{\alpha})], \tag{8}$$

$$\kappa = \frac{\alpha\gamma - \beta^2}{2(\gamma - \alpha)\beta^2}, \tag{9}$$

where a, b and γ denote the birefringent characteristics of the crystals forming the filter and n_j is the retardation of the split element when φ=0. Moreover, Equation 7 and 8 can be rewritten as

$$n_m + n_q = n_j[1 + \frac{\varphi^2\kappa}{2}(\frac{1}{\gamma} - \frac{1}{\alpha})], \tag{10}$$

$$n_m - n_q = \frac{n_j\varphi^2\kappa}{2}(\frac{1}{\gamma} + \frac{1}{\alpha})\cos 2\theta. \tag{11}$$

We can see that Equation 10 is equivalent to a simple wide-field Lyot's element. Hence,

$$n_m + n_q \approx n_j. \tag{12}$$

If we further assume that the filter is made of quartz, then

$$\kappa = \frac{1}{2\alpha}, \tag{13}$$

$$\mu = \gamma - \alpha << 1. \tag{14}$$

Because both α and γ are larger than 1, we can obtain

$$\frac{1}{\alpha} \approx \frac{1}{\gamma}, \tag{15}$$

Let $\delta = n_m - n_q$, then according to Equation 11, 13 and 15,

$$\delta = \frac{n_j \varphi^2 \cos 2\theta}{2\gamma^2}. \tag{16}$$

2.3 Characteristics of integrated transmission

Inserting Equation 5, 6 and 12 to Equation 1, we can obtain

$$\tau = \sin^2 2\pi n \sin^2 \pi\delta + \cos^2 2\pi n \cos^2 \pi n. \tag{17}$$

Then, the integrated transmission

$$T = \int_{n_0 - 1/2}^{n_0 + 1/2} \tau dn = \frac{1}{4} + \frac{1}{2} \sin^2 \pi\delta, \tag{18}$$

where n_0 is the desired retardation of the split element. Note that in Equation 18 we have omitted the change of δ with wavelength. The reasonableness of this assumption is: During one integrated period, the change of δ is

$$\Delta\delta = \frac{\varphi^2 \cos 2\theta}{2\gamma^2} \tag{16'}$$

and independent upon the value of n_j. The maximal value of Δδ has an order of 7.0×10^{-5} and is too small to be considered even if assuming the incident angle φ to be larger than 60'.

From Equation 18, we know that the integrated transmission of split-element filter is not conservative in its field of view. If φ does not change, the brightness varies periodically depending upon θ,

$$T_{\min} = \frac{1}{4}, \qquad \text{when } \theta = \frac{k\pi}{2} + \frac{\pi}{4}; \tag{19}$$

$$T_{\max} = \frac{1}{4} + \frac{\sin^2 \pi\delta}{2}, \qquad \text{when } \theta = \frac{k\pi}{2}, \tag{20}$$

where k is integer. And if θ does not change, the brightness distribution is limb-brightening,

$$T_{\min} = \frac{1}{4}, \qquad \text{when } \varphi = 0; \tag{21}$$

$$T_{\max} = \frac{1}{4} + \frac{\sin^2 \pi\delta}{2}, \qquad \text{when } \varphi \text{ is maximum.} \tag{22}$$

All of these phenomena are represented in Fig. 2.

At last, we simply discuss the integrated transmission of Lyot's filter in order to compare with split-element filter. We assume that the filter is equivalent to the split-element filter discussed above. After considering the off-axis effect, we can obtain the retardation of the thinner element,

$$n_j = n(1 + \frac{\varphi^2 \cos 2\theta}{2\gamma^2}) = n + \delta . \tag{23}$$

The integrated transmission

$$T = \int_{n_0 - 1/2}^{n_0 + 1/2} \cos^2 \pi(n + \delta) \cos^2 2\pi n dn = \frac{1}{4} . \tag{24}$$

Thus the integrated transmission of Lyot's filter is conservative and the inhomogeneity of brightness distribution does not exist.

In the above discussion, we don't consider the off-axis effect of the middle element. In fact, the conclusion of Eq.18 and 24 will not be changed even if considering the effect of the middle element in case of omitting the very small change of δ.

2.4 Quantitative calculation of inhomogeneous brightness distribution

One split-element unit was used in the 10cm Full Disc Solar Magnetic Field Telescope installed at Huairou Solar Station, Beijing Astronomical Observatory. This unit is made of quartz and the retardations of the split and middle element are 800 and 1600, respectively. Fig.2 shows its brightness morphology. Table 1 is an example of quantitative calculation when $\theta = k\pi/2$ and φ varies from 0 to 100'. Column 1 is obtained from Equation 18 and Column 2 is obtained by direct integration of Equation 17. From this table we can find that the larger the field of view is, the more serious the inhomogeneous

brightness distribution is. The differences between Column 1 and Column 2 are very small, so the assumption of Equation 18 is reasonable.

2.5 Effects of inhomogeneous distribution for astronomical observations

Since the brightness distribution is inhomogeneous in split-element filter, we have to study its property in detail. Here we define the brightness fluctuation as

$$\Delta T = \frac{T_{(\varphi,\theta)} - T_{(\varphi=0)}}{T_{(\varphi=0)}} . \qquad (25)$$

In our full disc solar telescope, the incident lights are collimated beams and the angular magnification is 4, and thus the maximal angle of the field of view is 64'. In this case, the maximal brightness fluctuation is about 9.44%. This inhomogeneity of brightness is large enough to distort the real morphology of observed object, increase stray light and affect the accuracy of magnetic field measurement, *etc*. For these reasons, the off-axis effect must be considered when we use split-element filter.

3. Discussion

The off-axis effect in split-element filter has been discussed in Section 2. We find that the larger the field of view is, the more serious the inhomogeneous brightness distribution is. Naturally, such inhomogeneity can be avoided if the split element is also wide-field element. A unit of wide-field split-element filter and its equivalent Lyot's filter are shown schematically in Fig.3a and 3b. In Fig.3, we can find that saving a polarizer is at the price of adding five achromatic waveplates in split-element filter. At present time, condition is a little different from that time when Evans invented split-element filter. In optical region, the transmission of polarizer can be higher than 90% if the incident light is polarized and not reflected, and its price is much cheaper than that of achromatic waveplate. Therefore, it is not suitable any more to add five achromatic waveplates for saving one polaroid.

At last, we must emphasize that we do not deny the usefulness of split-element filter, because the transmission of polarizer is still very low in UV, infrared, and other wavebands.

Split-element filter has its superiority over Lyot's filter in these wavebands, so we only conclude that it must be careful when we use split-element filter.

Reference

J. Evans, 'The Birefringent Filter', *J. Opt. Soc. Am.*, **39**, 229-242 (1949).

J. Evans, 'The Birefringent Filter: Correction', *J. Opt. Soc. Am.*, **39**, 412(1949).

A. M. Title and W. J. Rosenberg, 'Improvement In Birefringent Filter', *Applied Optics*, **18**, 3443-3456 (1979).

Captions

Figure 1: Structure of Split-element Filter

m and *q*: split element, *p*: middle element,

$\mathbf{P}_1$, $\mathbf{P}_2$ and $\mathbf{P}_3$: polarizer

(a). one unit of split-element filter

(b). Lyot's filter equivalent to split-element filter

Figure 2: Brightness Morphology of Split-element Filter

θ: the azimuthal angle of incident light

Figure 3: Wide-field Split-element Filter

$\lambda/2$: half achromatic waveplate

$\lambda/4$: quarter achromatic waveplate

(a). wide-field split-element filter

(b). equivalent wide-field Lyot's filter

Table 1: Integrated Transmission of a Split-element Filter in Different Incident Angle

$n_j = 800, \quad \theta = \pm k\pi, \quad \gamma \approx 1.55$

Column 1: calculated from Equation 18

Column 2: calculated by direct integration of Equation 17

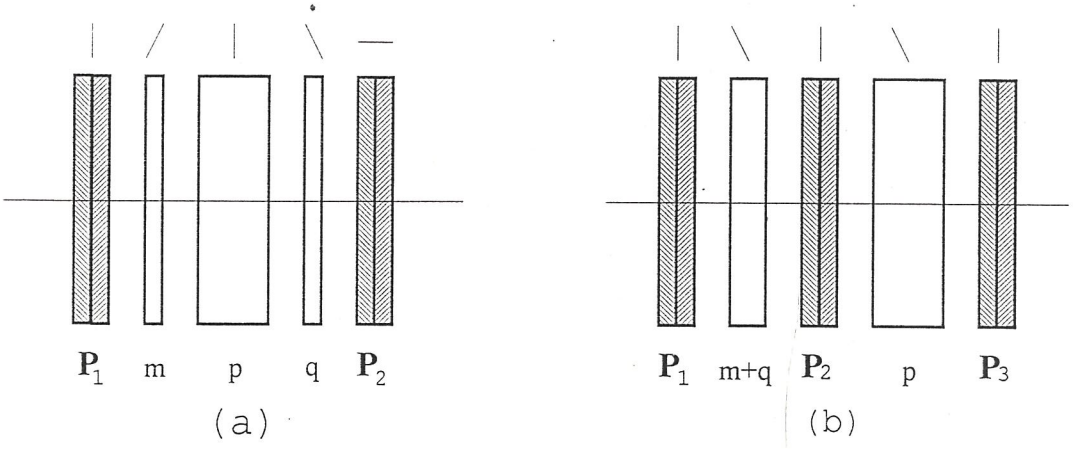

Fig.1 Structure of Split-element Filter

(a). a unit of split-element filter

(b). equivalent Lyot's filter

Field of view φ	Column 1	Column 2
0	0.25	0.25
10'	0.2500121	0.2500121
20'	0.2501621	0.2501623
30'	0.2508116	0.2508126
40'	0.2525575	0.2525607
50'	0.2562254	0.2562333
60'	0.2628493	0.2628652
70'	0.2736280	0.2736571
80'	0.2898520	0.2899005
90'	0.3127860	0.3128613
100'	0.3435019	0.3436112

Table 1. Integrated transmission of a split-element unit

n_j=800, r≈1.55, θ=±kπ/2

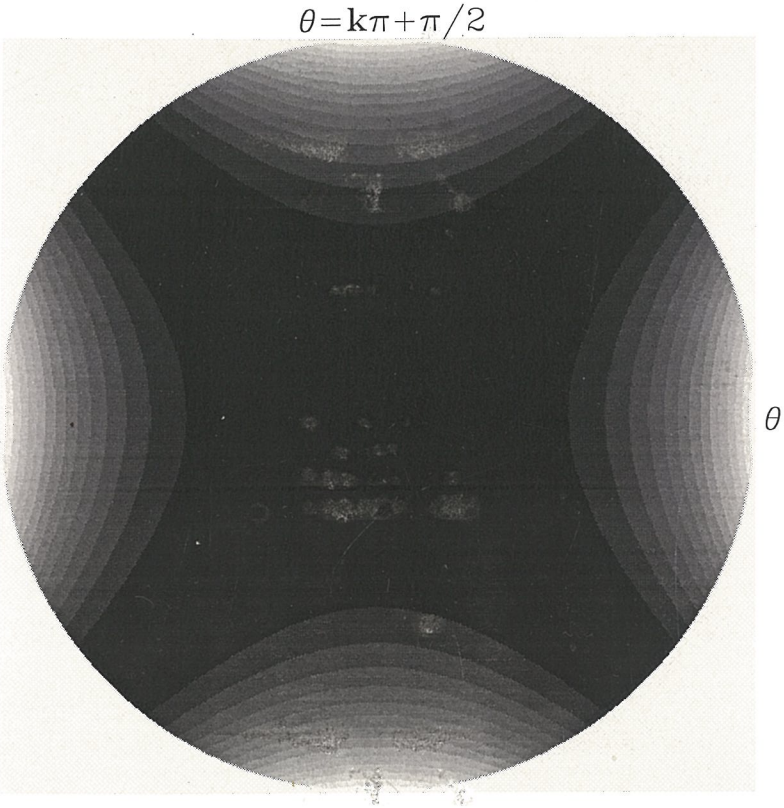

Fig.2 Brightness Morphology of Split-element Fliter

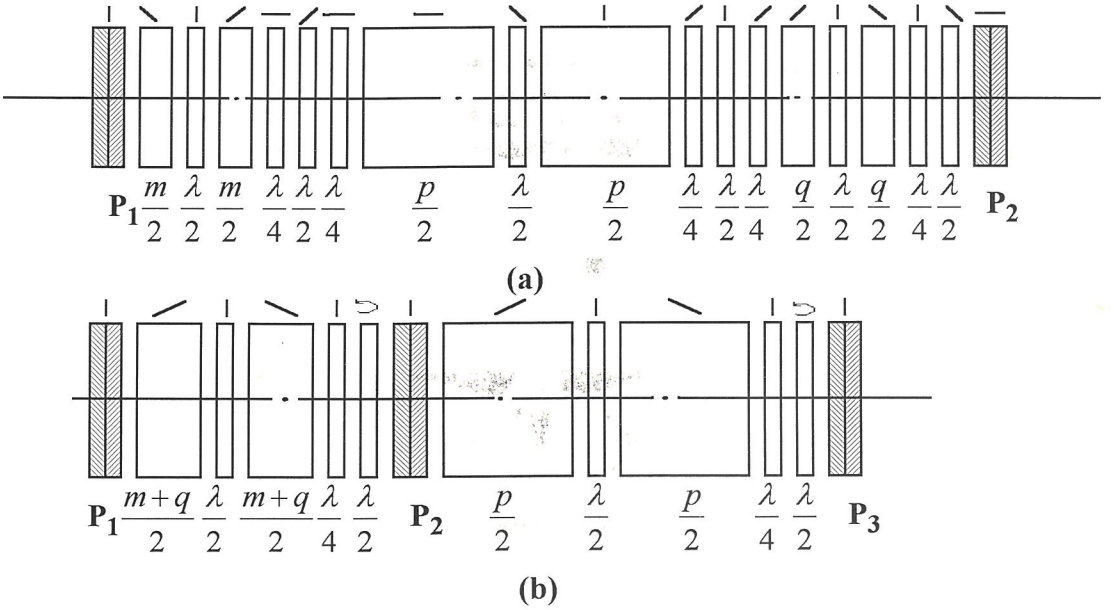

Fig.3 Two Types of Wide-field Filters

λ/2: half achromatic waveplate
λ/4: quarter achromatic waveplate
(a). split-element filter (b). Lyot filter

PART II

High Resolution Solar Telescope With MCST

Chapter 4

Introduction

One of the eternal topics in solar physics is to resolve the objects as fine as possible. In my knowledge, the ultimate goal in this century is to directly measure the magnetic fields with a spatial scale of about 0".1. This is because, on the one hand, the small-scale magnetic fields with this size relate to some fundamentals of solar physics (c.f. Solanki 1993); on the other hand, almost all ground-based telescopes currently used cannot achieve 0".1 spatial resolution due to the turbulence of the earth atmosphere.

Theoretically, the larger the aperture of a telescope, the higher the capability to resolve the objects. However, astronomical observations are limited by many actual conditions, one of which is the earth atmosphere. The turbulence of the atmosphere can cause the movement, distortion, blur and twinkling of the observed objects; consequently the spatial resolution will be lowered. The atmospheric turbulence can be represented by the Fried parameter (Fried 1966). As an empirical conclusion the long-term average Fried parameter in most solar observational bases is not better than 10cm, which corresponds to a spatial resolution of about 1".0 in the visible region. This resolution is too low for the observations of the small-scale structures. Thus, how to remove the effect of the earth atmosphere is the first key in high resolution solar observations.

Traditionally, solar observers choose excellent sites and wait good seeing in order to obtain high resolution data. Though quite simple and easy, these ways are so passive that they succeed only by chance, and these casual observations can hardly satisfy the requirements of modern solar physics. In the past thirty years many new instruments, such as correlation tracker, real-time image selector and adaptive optics, and new methods, such as image recovery, magnetic line-ratio, have been applied in solar observations. By means of these ways great progress has been made in the research of small-scale solar structures.

The cross-correlation method is a quite effective means to test the linear movement between two similar images. Correlation tracker system is based on this idea (von der Luhe *et al.* 1989). With this kind of instrument one can correct the movement among a successive images if they are taken within a time much shorter than the time scale of the object variation. The correlation tracker is especially useful for the observations which require long exposure,

such as the measurement of solar magnetic fields. In case long exposure is not required, a real-time image selection system has unique functions (Scharmer 1989). For an image, the higher the resolution in spatial domain, the stronger the power spectrum of high frequency in frequency domain. With this characteristic a real-time image selection system can select the best image from a set of images. The adaptive optics, to a certain content, is equivalent to a group of correlation tracker and thus some non-linear effects of the atmosphere can be tested and corrected by this technique (Acton 1989). The advantage of the above three kinds of instrument is that they correct the atmospheric effects almost at the same time while the observation is being carried out. On the other hand, there are some disadvantages: the technology to make these instruments is extremely complex; only part effects of the earth atmospheric turbulence can been removed. In addition to these instruments, some post-process methods are also applied in high resolution solar observations, two of which are speckle interference image recovery (SIIR) (von der Luhe 1984) and magnetic line-ratio (MLR) (Stenflo 1973) methods. The basic principle of the SIIR method is that if the exposure time is short enough, high resolution information can be remained in the images which have been distorted by the turbulence of the earth atmosphere. The advantage of this method is that the image with a resolution up to the diffraction limit of the telescope can be obtained; the disadvantage is that it requires a large amount of data and computational time. The MLR technique is based on the real-time observation at two or more wavelengths. These wavelengths should be selected with special care to ensure that the effect of the concerned parameter of the unresolved solar magnetic structures is separated from the effects of other parameters. By this way some physical parameters of the solar atmosphere, such as the strength of magnetic field, temperature and velocity, whereas not an image, can be obtained.

In the wake of development in instruments and methods, a great deal of progress has been made in the observation and study of small-scale solar structures during the past thirty years. It is beyond this thesis to review the research progress in this field, but I still would like to mention several important results. With the SIIR method, Keller (1992) resolved a magnetic elements with a FWHM of about 0."3 and Denker and de Boer (1996) got an image of granulation with a spatial resolution of about 0."16. As I know, they are the best

spatial resolution achieved in the ground-based solar telescope. With the MLR method Stenflo (1973) concluded that most magnetic flux (>90%) of the solar photosphere are in forms of KG discrete structures. Following Stenflo's conclusion is a long-term debate (Stenflo 1993; Zirin 1993). Till today the results disproving this view (before 1993, c.f. Zirin 1993; Keller 1994; Wang *et al.* 1996) are almost as many as those supporting it (before 1993, c.f. Stenflo 1993; Bruls and Solanki 1995).

The Multi-Channel Solar Telescope (MCST) (Ai and Hu, 1987a, b and c) has unique advantages for high resolution solar observations. During the recent four years I have being devoted myself to experiment the techniques and methods in observing small-scale solar structures with this telescope. In the following two chapters I will introduce some preliminary results. In Chapter 5, with the SIIR method I get a white-light image of granulation with a resolution better than 0."5 and r.m.s brightness contrast about 14%. In Chapter 6 I study the intrinsic properties of the magnetic elements in network and plage regions with the MLR method. This is the first time that the MLR method is used to analyze the real-time magnetograms obtained with a videomagnetograph. By a simple calibration I find that on the one hand, the magnetic fields of plage, enhanced network and quiet network are intrinsically strong; on the other hand, their strengths trend to decrease from active regions to quiet regions. I also find that there is no obvious correlation between the intrinsic field strengths and the magnetic filling factors.

References

Acton, D. S., 1989, in: *High Spatial Resolution Solar Observations*, von der Luhe (*eds.*), 71

Ai, G., and Hu, Y., 1987a, *Science in China*, p.868

Ai, G., and Hu, Y., 1987b, *Science in China*, p.1969

Ai, G., and Hu, Y., 1987c., *Acta Astrophysica Sinica*, 7, 305

Bruls, J. M. H. J. and Solanki, S. K., 1995, *A&A*, **293**, 240

Denker, C. And de Boer, C. R., 1996, *Solar Phys.*, **167**, inside front cover

Fried, D. L., 1966, *J. Opt. Soc. Am.*, **56**, 1372

Keller, C. U., 1992, *Nature*, **359**, 307

Keller, C. U., Deubner, F. L., *et al.*, 1994, *A&A.*, **286**, 626

Solanki, S. K., 1993, *Space Sci. Rev.*, **63**, 1

Scharmer, G. B., 1989, *NATO ASI Series* C, **263**, 161

Stenflo, 1973, *Solar Phys.*, **32**, 41

Stenflo, J. O., 1993, *IAU Colloq.*, **141**, 205

von der Luhe, O., 1984, *J. Opt. Soc. Am. A*, **1**, 510

von der Luhe, O., Widener, A. L., *et al.*, 1989, *A&A*, **224**, 351

Wang, J. X., Wang, H. M., *et al.*, 1995, *Solar Phys.*, **160**, 277

Zirin, H., 1993, *IAU Colloq.* **141**, 205

Chapter 5

High Resolution Image Recovery in the Quiet Region of the Sun

Acta Astronomica Sinica, 1994, Vol. 35, No. 4

Abstract

In this article we report some preliminary results obtained with the speckle interference image recovery (SIIR) method in the 60cm Multi-Channel Solar Telescope (MCST) installed at Huairou Solar Observation Station, Beijing Astronomical Observatory. In our observations, we collect a sequence of white-light images of solar granulation located at the disk center when the atmospheric turbulence of the earth is "frozen" by the exposure shorter than 10ms. After processing these data with the speckle-masking method, one of the SIIR methods, we reconstruct an image in which some granules smaller than 0."5 are resolvable.

1. Introduction

What do the fine structures of the solar photosphere look like? This is a very important and far from solved problem in solar physics. One of the keys to answer this question is to get observational data with high spatial resolution. However, a ground-based solar telescope can hardly obtain data with resolution higher than 1."0 due to the turbulence of the earth atmosphere. Thus, the first topic in high resolution solar observations is how to overcome the effects of the earth atmosphere.

There are some ways to remove or avoid the atmospheric effects, three of which are space telescope, adaptive optics and image recovery. Space telescope is the most direct and effective way and some of this kind of instruments are being realized. However, there still are some problems at present time. For example, the cost of space telescope is very high and the operation and renewal are quite inconvenient. Adaptive optics is to add some correction systems changing with the earth atmosphere into the telescope. Similarly to space telescope, this method is used only in several systems (Peri et al. 1989; Scharmer and Lofdahl 1991) due to its very difficult technology. Theoretically, image recovery method is not so perfect as the above two methods. Even so, it is broadly used in astronomy because it can be easily realized with present technology. It is a post-process method being carried out after the data is recorded. This method requires high speed image collectors (such as CCD cameras), real-

time data storage and rapid and large-capacity computer. These requirements are not too difficult to be achieved at present.

In this paper we will introduce the application of one of the image recovery methods, the speckle interference image recovery (SIIR) method, in the 60cm Multi-Channel Solar Telescope (MCST). Some preliminary results will be given too. In Section 2 we briefly introduce the effects of the earth atmosphere and some pre-process methods used in the SIIR. The detail of the SIIR will be described in Section 3. In Section 4 we introduce the hardwares and in Section 5 summarize the results.

2. Effects of the earth atmosphere and pre-process methods in the SIIR

It is well known that the turbulence of the earth atmosphere can cause the movement, distortion, blur and twinkling of the astronomical objects, and consequently the spatial resolution of a telescope is lowered. The key of the image recovery method is how to remove the atmospheric effects from the distorted images. The basis of the SIIR method is to replace a long exposure image with a set of images in each of which the exposure time is shorter than the characteristic time scale of the atmospheric turbulence (about 10ms). In case of short exposure, the earth atmosphere can be "frozen" and high resolution information can be remained in these "short exposure" images. The movement between two images can be corrected with the cross-correlation method. The pre-process also includes the flat field and dark current correction. However, it is not so easy to correct most of the atmospheric effects, such as the distortion and blur. In fact it is what should be solved with the SIIR method.

It is the random turbulence of the atmosphere that lowers spatial resolution, on the other hand, just by means of some statistic characteristics of this random process we can reconstruct the image quite similar to the real objects from the distorted images.

3. Development and application of the SIIR method

3.1. history of the SIIR

The SIIR method was firstly introduced into astronomy by A. Labeyire, a French astronomer, in 1970 (Labeyire 1970). By this way he obtained the power spectrum of the observed objects with high spatial resolution. In the following years many astronomers greatly contributed to the development of this method (Knox and Thompson 1974; Knox 1976; Weigelt 1977; Weigelt and Wirnitzer 1983) and established several data analyzing and processing systems, such as the Knox-Thompson (KT) technique (Knox and Thompson 1974) and Speckle-Masking (SM) technique (Weigelt and Wirnitzer 1983). By means of these techniques a great deal of results had been made on stellar observations (Balega et al. 1984; Foy et al. 1985; etc.). In 1980's scientists began to discuss the possibility to observe the Sun with the SIIR method. The biggest problem for solar observations is how to find the reference stars. As one knows, it is almost impossible to find such a star because the Sun is so bright that all stars cannot be seen in the daytime. Using a half-empirical model of the earth atmosphere, the log-normal model (Korff 1974), von der Luhe found a way to partly solve this problem (von der Luhe 1984). From then on the SIIR methods was broadly applied in solar observations. Recently Keller and von der Luhe promoted the research of this field to a new level. They have reconstructed some small-scale magnetic structures (Keller et al. 1992; Keller and Von der Luhe 1992).

In this paper we recover the images of solar granulation obtained by the MCST with the SM method. Our purpose is to establish and perfect the hardwares and test the softwares for the application of this method in our telescope. To a certain content, the present work is a preparation of the study of small-scale magnetic fields with the SIIR method in the MCST. Making use of the advantages of the MCST and the SIIR method, we expect to get some excellent results in the future.

3.2. principle of the SM method

As we know, when the light from the observed object is received by a detector after it passes through the atmosphere and telescope system, the imaging formulation is

$$I_{(\vec{x})} = A_{(\vec{x})} * O_{(\vec{x})} \qquad (1)$$

in the spatial domain, and

$$\widetilde{I}_{(\vec{u})} = \widetilde{A}_{(\vec{u})} \widetilde{O}_{(\vec{u})} \qquad (2)$$

in the frequency domain. In these formulations, $\vec{x}$ and $\vec{u}$ are the 2-D space and frequency vectors, I and O the 2-D intensity distribution of the image and the object, "~" denotes the Fourier transforms, "*" means convolution, and A is the transfer function of the atmosphere and telescope system. Thus, knowing the optical transfer function, $\widetilde{A}_{(\vec{u})}$, one can calculate the intensity distribution of the object.

Unfortunately, high resolution observations are not so easy as what is shown in the above equations, because one cannot exactly describe the optical transfer function of the earth atmosphere at present time. A currently popular way is to recover the modulus and phase of the Fourier transform of the object with different methods. This has proven quite successful. In the following we will simply introduce the principle of the SM method in which the bispectrum is used to recover the phase of the object's Fourier function. Before this introduction we would like to note that each variable used here is the parameter in case the atmosphere is frozen by short exposure (<10ms), and the average of the variable during the total sample time is represented by the symbol of "<>".

Phase recovery. The recovery of phase is achieved with the bispectral algorithm. The bispectrum, $S^{(3)}_{(\vec{u},\vec{v})}$, of a function, $S_{(\vec{u})}$, is defined as

$$S^{(3)}_{(\vec{u},\vec{v})} = S_{(\vec{u})} S_{(\vec{v})} S_{(-\vec{u}-\vec{v})}. \qquad (3)$$

From Eq. (2) we can reform the imaging formulation with bispectrums:

$$\left\langle \widetilde{I}^{(3)}_{(\vec{u},\vec{v})} \right\rangle = \left\langle \widetilde{A}^{(3)}_{(\vec{u},\vec{v})} \right\rangle \widetilde{O}^{(3)}_{(\vec{u},\vec{v})}, \qquad (4)$$

where, each parameter has been averaged and the object is assumed unchanged within the sample time. Weigelt et al. (1983) proved that the average bispectrum of the atmospheric optical transfer function, $\left\langle \widetilde{A}^{(3)}_{(\vec{u},\vec{v})} \right\rangle$, is a real function in the log-normal model of the earth

atmosphere. In this case we can obtain a recursive expression of the object's phase,

$$\alpha_{(\vec{u}+\vec{v})} = \alpha_{(\vec{u})} + \alpha_{(\vec{v})} - \beta_{(\vec{u},\vec{v})}, \qquad (5)$$

where, α represents the phases of the object and $\beta_{(\vec{u},\vec{v})}$ the phase of the image's bispectrum. Because the phase of the image can be calculated from the observational data, that of the object can be deduced by Eq. (5).

Modulus recovery. The recovery of modulus is achieved by the method of speckle interferometry Labeyire firstly applied in astronomy. The modulation transfer function (MTF) of the earth atmosphere is used in this method. For stellar observations, the MTF can be obtained by observing an unresolvable star at the time when and in the field of view where the object is observed. For solar observation, it is impossible to find such a reference star because the Sun is too bright. In this case, some other ways are applied. At first, let's see a variation of Eq. (2):

$$\left\langle \left| \tilde{I}_{(\vec{u})} \right|^2 \right\rangle = \left\langle \left| \tilde{A}_{(\vec{u})} \right|^2 \right\rangle \left| \tilde{O}_{(\vec{u})} \right|^2, \qquad (6)$$

where, "||" represents the algorithm of the modulus and $\left\langle \left| \tilde{A}_{(\vec{u})} \right|^2 \right\rangle$ is the MTF of the atmosphere and telescope system. Korff (1974) indicated that the MTF is determined only by the atmospheric Fried parameter for a given telescope in the log-normal atmospheric model. Thus, how to recover the modulus is changed to how to measure the Fried parameter. von der Luhe introduced a spectral ratio method to estimate this parameter (Von der Luhe, 1984). The function of spectral ratio, $\varepsilon_{(\vec{u})}$, is defined as

$$\varepsilon_{(\vec{u})} = \left| \left\langle \tilde{I}_{(\vec{u})} \right\rangle \right|^2 \Big/ \left\langle \left| \tilde{I}_{(\vec{u})} \right|^2 \right\rangle, \qquad (7)$$

In this formulation, the numerator is the power spectrum of long exposure image which rapidly drops off to zero at the frequency of r_0/λ, where r_0 is the Fried parameter and λ the wavelength, while the denominator does at the frequency of the diffraction limit of the telescope. Due to this property the spectral ratio will sharply drop off at the frequency of r_0/λ (Fig. 1). Thus, from the curve of the spectral ratio one can determine the Fried parameter and furthermore the atmospheric MTF. By this way the modulus of the object can

be recovered.

Finally, the real object can be constructed by an inverse Fourier transform.

4. Hardwares of the SM method in the MCST

Detector. As mentioned above, the basis of the SIIR method is to replace the long exposure with a set of short exposure, so the first key is to equip detectors with high speed exposure function. We used a HDBW-9207 CCD camera, whose electric shutter can be changed from 0.1ms to 20ms and sample rate is 25 frames per second. The elements of the sensor is 795×596 and the size $7.95\text{mm} \times 6.45\text{mm}$. The data is transferred in interlace mode.

Data storage. In addition that the atmosphere should be frozen, the ergodic hypothesis should be satisfied too in the SIIR method. The ergodic hypothesis has two requirements, one is enough long time interval between two samples, the other is enough large number of samples. The first requirement is automatically satisfied by our CCD camera. The later must be carefully considered because it means enough long observational time at a fix sample rate. In the above section we have treated the object as an unchanged parameter; on the other hand, whenever the solar structures evolute or vary, if the observational time is too long, we cannot consider them unchanged. In our system, the observation takes 30s and thus 750 frames can be recorded. It must be noticed that we cannot ensure the object entirely unchanged within 30s, but we have to do so in order to collect enough samples. The data is stored by a TMT real-time disk, whose capacity is 1GB corresponding to 3000 white-light images in Huairou's data format.

Image processor. The ITEX 151 image processor is used. its pixel number is 512×512. If 36m focal length is used, the synthetic spatial resolution of the CCD camera and image processor is $0.''089 \times 0.''0625$/pixel.

Computer. Because two-dimensional vector is expanded to four-dimensional vector in

the calculation of bispectrum, the amount of calculation is quite large. In this case a rapid and large-capacity computer is necessary. Nowadays we use a Sun SPARC Station 400.

5. Results and discussions

In Huairou Solar Station, excellent whether for solar observation often occurs in May and June. On June 04, 1993, we took some speckle images at $\lambda 5250 \pm 50$ in the 60cm MCST. Fig. 2 is a result of granulation at the disk center. In this figure, **a** is the long exposure result obtained by directly integrating all the speckle samples and has quite low resolution, **b** is one of the best speckle samples, **c** is long exposure image in which every sample is corrected with the cross-correlation method, and **d** is the image reconstructed by the SM method. By the spectral ratio method we estimate the Fried parameter during our observations was about 82mm. Fig. 3 is combined by three segments such as Fig. 2(b) and 2(d). The conclusions based on Fig. 2 and Fig. 3 are summarized in the following.

From Fig. 2(a) and (c) one can see that the cross-correlation method is very effective to correct image's movement caused by the earth atmosphere. Fig. 2(b) demonstrates that the distortion and blur still exist even if the atmosphere has been frozen; on the other hand, high resolution information is remained too. Compared with Fig. 2. (b), Fig. 2(d) has higher spatial resolution. We conservatively estimate that the resolution in Fig. 2(d) is not worse than 0."5. The diffraction limited resolution of a 60cm telescope at the wavelength of $\lambda 5250$ is about 0."16, thus the resolution in Fig.2 is much lower than what it should be. This is because in the samples there is a periodic noise with frequency of about 0."5 and in order to remove it we have to smooth each image at the spatial scale of 0."5. Where does the noise come from? By our later experiments we think it comes from the CCD camera itself. Thus we intend to use some new kind of CCD cameras in the future.

In the reconstructed images of Fig. 2 and 3, we can easily find the characteristics of granulation: most granules are smaller than 2."0; there are many dark lanes among the granules; the r.m.s. brightness fluctuation calculated with statistic method is about 6% for

direct integration, 8% for the integration after cross-correlation, 10% for speckle sample and 14% for the reconstructed image. All of these results are agreement with the traditional knowledge about solar granulation (Muller, 1989).

Acknowledgments

The authors are grateful to Mr. Wang Tongjiang for his help and discussions. We also thank Prof. Zhang Hongqi and other colleagues in Huairou Solar Station for their discussions. One of the authors, Deng, would like to thank Prof. Hirayama, National Astronomical Observatory of Japan, for his encouragement.

References

Balega, Y., Bonneau, D., and Foy, R., 1984, *A.&A. Sup. Ser.*, **57**, 31

Foy, R., Bonneau, D., and Blazit, 1985, A., *A.&A.*, **149**, 13

Keller, C. U., O. von der Luhe, and Stenflo, J. O., 1992, *A.&A.*, **254,** 355

Keller, C. U. and O. von der Luhe, 1992, *A.&A.*, **261**, 321

Knox, K. T. and Thompson, B. J., 1974, *Ap. J.*, **193**, 45

Knox, K. T., 1976, *J. Opt. Soc. Am.*, **66,** 1236

Korff, D., 1974, *J. Opt. Soc. Am.*, **64**, 1129

Labeyire, A., 1970, *A.&A.*, **6**, 85

Muller, R., 1989, *NATO ASI Series C*, **263**, 101

Peri, M. L., Smithson, R. C., et al., 1989, *NATO ASI Series C*, **263**, 77

Scharmer, G. and Lofdahl, M., 1991, *adv. Space Res.*, **11**, 129

von der Luhe, O., 1984, *J. Opt. Soc. Am.*, **A1**, 510

Weigelt, G., 1977, *Opt. Comm.*, **21**, 55

Weigelt, G. and Wirnitzer, 1983, *Opt. Lett.*, **8**, 389

Captions

Figure 1. The observed curve of spectrum ratio

a. y=0 b. y=x

c. x=0 d. y=-x

where, (x, y) is the coordinate of power spectrum in frequency domain, the initial point, (0, 0), corresponds the 'zero frequency' point.

Figure 2. Results of image recovery

(a). "long exposure" image obtained by directly integrating all samples

(c). "long exposure" image, each sample has been corrected by cross-correlation method

(b). a speckle sample

(d). the reconstructed image

Figure 3. the reconstructed image consisting of three images shown in Fig. 2.

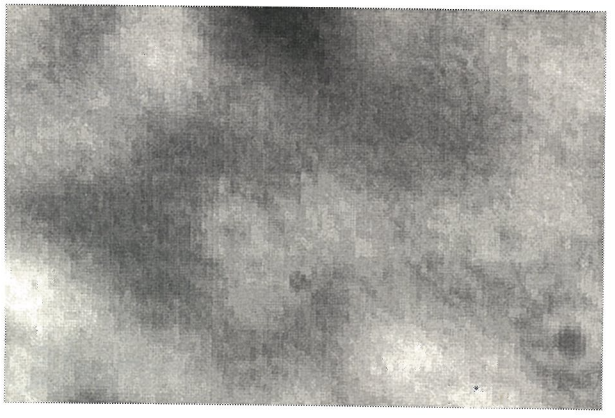

a. direct average

b. speckle sample

c. correlation then average

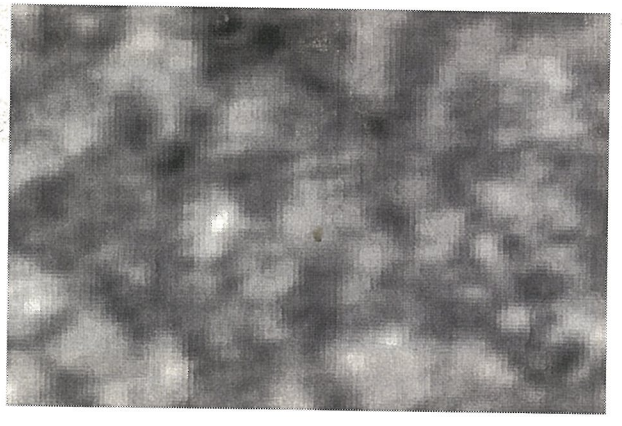

d. reconstruction image

Figure 1. Results of speckle interference image recovery

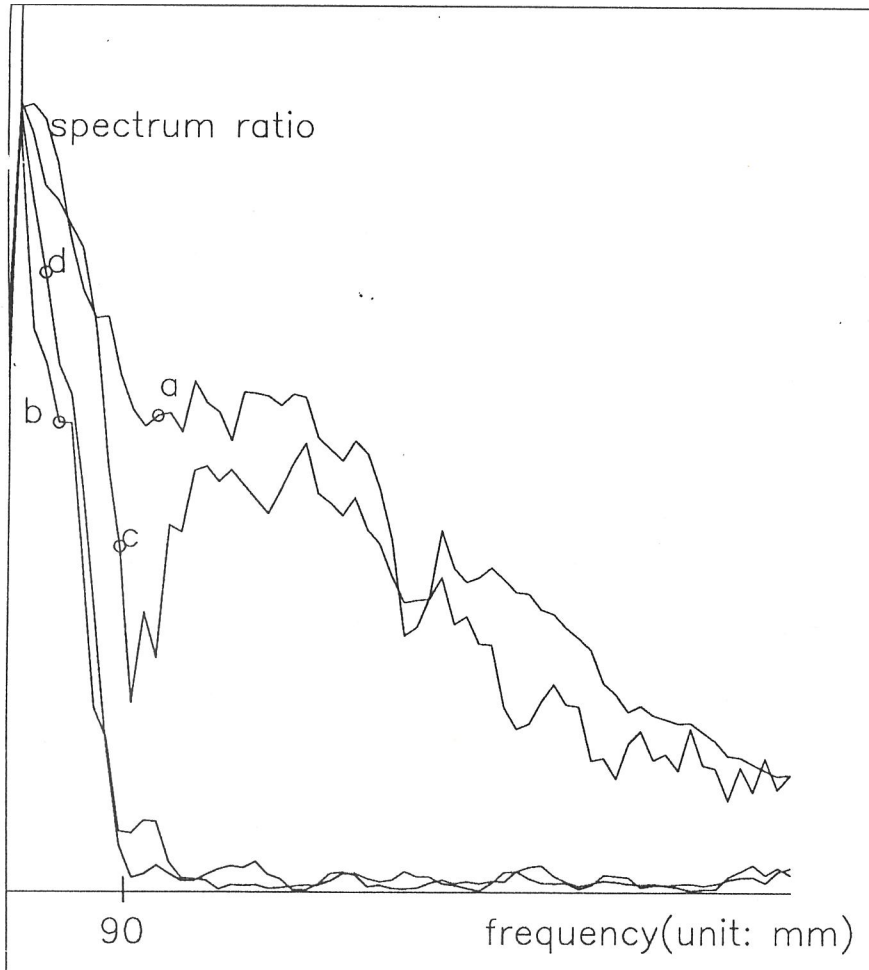

Fig.2 CURVE OF SPECTRUM RATIO

a. y=0 b. y=x
c. x=0 d. y=−x

Field of view : 29.3*13.6 arcsec

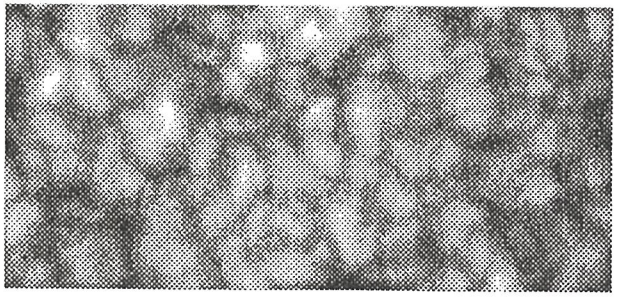

(a). speckle sample

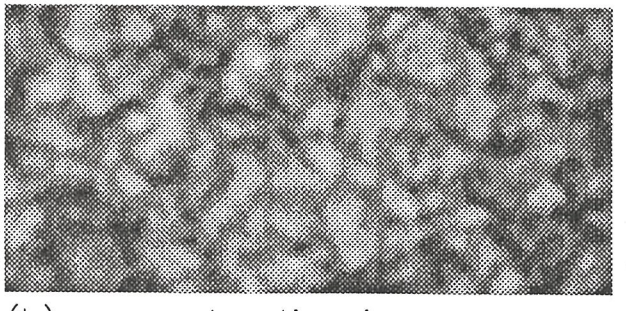

(b). reconstruction image made by three segments

Fig.3 COMPARSION BETWEEN SPECKLE AND RECONSTRUCTION IMAGE

Chapter 6

Intrinsic Strength of Network Magnetic Elements

Submitted to A&Ap.

Abstract

With the help of the Nine-Channel Solar Telescope (NCST), we have firstly applied the magnetic line ratio technique (MLR) to analyze the real-time longitudinal magnetograms of FeI5247.06 and FeI5250.22 obtained by filter system. In order to concentrate on the intrinsic properties of network magnetic element, we differ quiet network, enhanced network and plage from each other. By an analytical calibration method, we find that: a. The intrinsic magnetic strengths of quiet network elements vary from 689G to 1499G, while those of enhanced network and plage magnetic elements vary from 741G to 1976G and from 1343G to 1960G, respectively; b. Most of magnetic elements (forty-one of forty-seven) are intrinsically strong (>970G); c. The intrinsic field strengths trend to decrease from plage and enhanced network to quiet network. We also study the dependence of intrinsic magnetic strength upon filling factor, and find that no clear correlation exists between them

1. Introduction

It is well known that most of the magnetic flux outside sunspots and pores is concentrated into subsecond fluxtubes in solar photosphere. Unfortunately, these fluxtubes can hardly be resolved at the present time because the spatial resolution for solar magnetic field observation can hardly be higher than 1."0 due to the effects of earth atmosphere. That is to say we can only obtain the average magnetic flux over many individual fluxtubes and can not determine the intrinsic magnetic strength of single fluxtube by direct measurements of ground-based solar telescope.

Although direct observations are very difficult, many indirect techniques had been used to diagnoses small scale magnetic structures in the past thirty years. By these ways, many meaningful results had been obtained (*c.f.*, Solanki 1993). The magnetic line ratio (MLR) technique introduced by Stenflo (1973) is one of the most important and successful methods. In the MLR technique, Stenflo used the line pair of FeI5247.06 and FeI5250.22.

These two lines are formed in the same solar layer, belong to the same multiplet and are of equal strength. The only difference between them is the Lande factor. Thus, if recording the magnetic signals in this line pair simultaneously, one can separate the effect of intrinsic field strength from the effects due to line weakening and Doppler shift. By this way, Stenflo found that the intrinsic strengths of unresolved small scale magnetic structures outside sunspots are about 2000G. After this forerunning work, the MLR technique was extensively accepted and developed by many authors (Wiehr 1978; Stenflo and Harvey 1985; Solanki *et al.*, 1987; Sanchez *et al.*, 1988; Zayer *et al.*, 1990, Keller *et al.*, 1990, Keller *et al.*, 1994; *etc.*). For plage and enhanced network, these results had confirmed the famous 'strong field' view very well. The 'strong field' view suggests that more than 90% of the magnetic flux recorded by magnetograph is in strong-field, KG form (Howard and Stenflo 1972; Frazier and Stenflo 1972). Besides the MLR technique, many other methods had also confirmed this view (Tarbell and Title 1977; Frazier and Stenflo 1978; Ruedi *et al.*, 1992; Rabin 1992; Bruls and Solanki 1995; *etc.*). On the other hand, for intranetwork (IN), Keller (1994) found its intrinsic strength can hardly be higher than 1KG (only 5% probability). Keller's conclusion is in agreement with the conclusions obtained with videomagnetograph (VMG) (Martin 1988; Zirin 1987; Wang *et al.*, 1995; *etc.*) and disagreement with the 'strong field' view.

The previous results sited above seem to suggest that the intrinsic magnetic properties are different between relatively stronger magnetic regions (plages and enhanced networks) and relatively weaker regions (IN). How about are the intrinsic properties of quiet network? Many authors always tended to discuss quiet network undistinguished from enhanced network and plage, but we think it should not be neglected that there exist some differences among quiet network, enhanced network and plage. Thus, it is necessary to discuss the intrinsic magnetic field of quiet network separately. In this paper, we will isolate quiet network, enhanced network and plage from each other, and compare their intrinsic magnetic properties by the MLR technique.

For the observations of solar magnetic fields, two types of instrument are broadly used: spectrometer and filter. The spectrometer system can work at very wide spectral range though its field of view is small; The filter system has large field of view but it can

only work at one wavelength at one time. Because the MLR technique requests real-time observation, it was mainly applied in spectrometer system in the past years. However, to a certain content, large field of view is as important as real-time observation. If one want to study small-scale magnetic structures in large field of view, filter system is the best candidate. Keller *et al.* (1990) firstly analyzed the filtergrams of FeI5247.06 and FeI5250.22 with the MLR technique. (As we know, this is the only example that the MLR technique was used in filter system.) By analyzing an active plage region near a sunspot, they found that the intrinsic strengths of plage magnetic elements are compatible with a unique value about 1000G at the level of line formation, and for a thin fluxtube model they are about 2000G at the level of continuum formation. This result is in agreement with the previous 'strong field' conclusion. Unfortunately, because their magnetograms were not obtained simultaneously, their technique is not 'ideal' MLR technique. Thus, in order to apply the MLR method in large field of view, a new type of solar instrument, which can work at wide spectral range and large field of view simultaneously, is expected. The Nine-Channel Solar Telescope (NCST) (Ai and Hu, 1987a, b and c), which is a filter system and can work at nine selected wavelengths simultaneously, provides us a real chance to do so.

In this paper, by analyzing the real-time magnetograms of FeI5247.06 and FeI5250.22 obtained by the NCST with the MLR technique, we study the intrinsic field strengths of network magnetic elements isolated from enhanced network and plage magnetic elements. In Section 2, we introduce the NCST simply; In Section 3, data preprocessing is introduced; In Section 4, we use the MLR technique to deduce the intrinsic strengths of magnetic elements in networks and plages; Conclusions and discussions are given in Section 5 .

2. Instrument

All of the data analyzed in this paper were obtained by the NCST. This telescope was put into operation by the end of 1994 (Deng *et al.*, 1995). Fig.1(a) shows its basic structure and Fig.1(b) shows the scheme of its universal birefringent filter. In Fig.1(b), PB is polarizing beam splitter, which can split one incident light into two emergent beams by their

polarizing directions, and AR is total reflection prism, which is used to maintain the exit beams parallel. The other optical elements used in this filter, such as achromatic waveplates, polaroids and birefringent crystals, *etc.*, are not drawn in Fig.1(b). The nine designed wavelengths are labeled at right side of Fig.1(b). One must note that each channel can be adjusted to work at any other interested wavelength in visible region because this filter is universal system. Thus, the NCST can work at nine selected wavelengths simultaneously. From Fig.1(b) one can see that only one birefringent element is different for the line pair FeI5247.06 and FeI5250.22. Because the FWHM of this element is about 3.2 and very wider than the filter's FWHM (about 0.046Å), we can expect that the signals of the line pair are affected by the same conditions before they are received by CCD cameras.

The observation is operated by PC computer. The signals from CCD cameras are processed by image processor at first, then the results are recorded into PC computer. When longitudinal magnetic fields are observed, the right and left circular polarized lights are chosen alternately by KD*P modulator at video rate. The magnetic signal S are recorded as

$$S = \frac{I_L - I_R}{I_L + I_R}, \qquad (1)$$

$$I_{L,R} = \int V_{L,R(\lambda)} F_{(\lambda,\Delta\lambda_0)} d\lambda , \qquad (2)$$

Where, V_L and V_R denote the profiles of left and right circular polarized light, F is filter's transmitted profile, and $\Delta\lambda_0$ is the distance of the filter's passband center apart from the spectral line center. The field strength can be deduced by

$$B = C \cdot S , \qquad (3)$$

Where, C denotes the calibration coefficient.

3 Observations and Data Reduction

Three sets of real-time longitudinal magnetograms of FeI5247.06 and FeI5250.22 will be analyzed in this paper. They were obtained in a quiet network region located at solar disc

center on Sep.15, in a plage region at μ=0.98 on Sep.27, and in an enhanced network region at disc center on Sep.13, 1995, respectively. Fig.2 shows these magnetograms of FeI5250.22. In this figure, all of the magnetic elements analyzed in this paper are marked and numbered. For the observations of longitudinal magnetic field in NCST, the sensitivity is highest when filter's passband is placed at the position of -0.045Åfrom line center, while the relation between magnetic signal and field strength is most linear at -0.06Å We chose the later mode in our observations. (Unfortunately, the passband was placed at -0.075 from line center by a mistaken operation when we observed the enhanced network region on Sep.13. This condition is considered in the following discussion.) The field of view is about 3.'7×2.'4, and the pixel size is about 0."45×0."38. It took 160s to finish an observation of longitudinal magnetic field. In this observational mode, the spatial resolution is mainly decided by the earth atmospheric conditions during the observations. For our magnetograms, the average spatial resolution is estimated to be 2".0. Accordingly, we smooth the magnetograms by 5×5 pixels in order to reduce noise.

Then, we choose a criterion of field strength and mark the magnetic elements whose apparent field strengths are stronger than the criterion. By this way we can isolate all magnetic elements from each other. For the magnetograms of FeI5250.22, the criterion is 26G for quiet network elements and 32G for enhanced network and plage elements. In this case, twenty-one magnetic elements of quiet network, eleven magnetic elements of plage and seventeen magnetic elements of enhanced network are marked (see Fig.2). In the following section, we will analyze the intrinsic properties of these isolated magnetic elements one by one.

4 Results

4.1 Intrinsic magnetic fields

At first we analyze the intrinsic field strengths of magnetic elements in networks and plages. The magnetic line ratio **R** is defined as

$$R = {}^{S_{5250}}\!/_{1.5S_{5247}}, \qquad (4)$$

where, the magnetic signal **S** is defined in Equation 1. By this equation we can calculate the value of magnetic line ratio of each pixel inside the marked magnetic element. The diagrams of line ratio *vs.* apparent magnetic strength are shown in Fig.3. In this figure, (a), (b) and (c) correspond to quiet network, plage and enhanced network, respectively. For each region, we always show two extreme magnetic elements, one is relatively larger and stronger, and the other one is smaller and weaker. We can see that the values of the observed magnetic line ratio in one magnetic element are compatible with a unique value, though it is randomly blurred by noise due to the photon statistics, the CCD cameras, and the earth atmospheric distortion, *etc.*. (In the left panel of Fig.3(b), there are three 'unique' values. This is not contradictory with our conclusion, because if we select the criterion of field strength more carefully, we can find that this element actually consists of three smaller magnetic elements whose magnetic line ratios correspond to the three 'unique' values one by one.)

Because unique value of magnetic line ratio corresponds to unique intrinsic field strength, we can conclude that the intrinsic magnetic strengths in one magnetic element are similar, no matter how different the apparent magnetic strengths are. Table 1 lists the average line ratio **R**, the r.m.s. estimation $\Delta\mathbf{R}$ of **R**, the intrinsic field strength $\mathbf{B_I}$ and the filling factor α of each magnetic element marked in Fig.2. From Fig.3 and Table 1 we can see that almost all the magnetic elements of networks and plages are intrinsically strong and most of them (forty-one of forty-seven) are stronger than 970G (see Subsection 4.2). This is coincident with the 'strong field' view. On the other hand, we have also noticed that the intrinsic field strengths trend to decrease from plage and enhanced network to quiet network.

4.2 Calibrating to the MLR technique

Usually, one has to assume some fluxtube models and solve the radiation transfer equations in order to determine the intrinsic magnetic strengths from the observed line ratio

R. In order to avoid so much complicate work, we use a rough but very simple calibration method in our work. In this method, we assume that the studied magnetic fields are 'pure' longitudinal fields, thus the circular polarized profile can be roughly expressed by the unpolarized intensity profile shifted $\pm\Delta\lambda$ from the line center. Here, $\Delta\lambda$ is the value of Zeeman splitting:

$$\Delta\lambda = 4.67 \times 10^{-13} gB\lambda^2 \ , \qquad (5)$$

where, g is the effective Lande factor. The unpolarized spectral profile is provided by Prof. Livingston and the filter's transmitted profile is calculated by its design parameters. After knowing the circular polarized profile and the filter's transmitted profile, we can determine the calibration curve of $\mathbf{B_I} \sim \mathbf{R}$ from Equation 1, 2, 4 and 5. Fig.4 shows the calibration curves when filter's passband is placed at the position of -0.06 (solid line) and -0.075Å (dash line) from line center. Then, we can deduce the intrinsic magnetic strength $\mathbf{B_I}$ by comparing the observed value of **R** with the calibration curve.

Obviously, this calibration method is far from exact, because the observed magnetic fields are not 'pure' longitudinal fields actually. However, it is a reasonable approximation to a certain extent because the direction of small-scale magnetic field always tends to be vertical to the solar surface (Lites and Skumanich 1990; Howard 1991; Sanchez and Pillet 1994; Bernasconi *et al.*, 1995). Thus, we can roughly estimate the field strength by this way if we carry out the observation in solar disc center.

In actual astronomical observations, the effects of stray light must be considered. In order to do that, we do such an experiment: At first, we assume that the normalized spectral profile is distorted by the stray light whose normalized value is 0.5 in any spectral position; Then, such 'distorted' profile is used to calculate the calibration curve by the same method described above. The result is also drawn in Fig.4 (dot line). It is very surprising that although the spectral profile is distorted very much, the calibration curve is affected very little. In fact, this result is not incomprehensible because the line pair are distorted by the same way. Thus, one can understand why the same observational condition is especially important in the MLR technique. Due to the same reason, the MLR technique can hardly be used in filter system, except in our NCST. On the other hand, we can see from Fig.4 that

the calibration curve is very sensible to the position of filter's passband, though it is not sensible to stray light.

About the value of magnetic line ratio, a normal view is that it is approximate unity for weak fields and decreases when the field strengths increase. This view is proper for the instruments based on spectrometer, because this kind of systems works at a finite passband and the linear relation between field strength and magnetic signal is very well when magnetic fields are weak. While it is not proper for the systems based on filter. In filter system, the magnetic signal is the convolution of the polarized light and filter's profile at very wide spectral range, so the relation between field strength and magnetic signal is not linear even if magnetic fields are weak.

By the calibration method introduced above, the intrinsic strengths of magnetic elements of network and plage can be determined. All of these results are shown in Table1. (We must notice that the field strengths of enhanced network are obtained at -0.075Åfrom line center, while those of plage and quiet network are obtained at -0.06Å However, this will not affect our conclusion very much.) We can see that for the magnetic elements of quiet network, the intrinsic strengths vary from 689G to 1499G, most of them (fifteen of nineteen) are higher than 970G; (The other two elements (NO.20 and 21 in Fig.2(a)) can not be determined because their line ratios are beyond the calibration curve.) For those of enhanced network, the intrinsic strengths vary from 741G to 1976G, most of them (fifteen in seventeen) are higher that 1000G; And for those of plage, the intrinsic strengths vary from 1343G to 1960G. That is to say that most of these magnetic elements are intrinsically strong. Furthermore, we also notice that the field strengths trend to decrease from plage and enhanced network to quiet network.

4.3 Filling factor α

After obtaining the intrinsic field strengths, we can deduce the magnetic filling factors of each magnetic element. The filling factor α is defined as

$$\alpha = \frac{B_A}{B_I} . \qquad (6)$$

Where, B_A is the average apparent field strength of each magnetic element. The results are also listed in Table1. In Fig.5, we draw the $\alpha \sim B_I$ curve (Fig.5(a)) and $\alpha \sim B_A$ curve (Fig.5(b)). We can see that there does not exist clear correlation between filling factor and intrinsic field strength, though filling factor trends to increase depending upon apparent magnetic strength.

5 Conclusion and Discussion

We want to emphasize again that this is the first time that the magnetic line ratio technique is used to analyze real-time magnetograms obtained by filter system. The characteristic of our work is that we study quiet network, enhanced network and plage separately. Our objectives contain a quiet network region consisting of twenty-one isolated magnetic elements, an active plage consisting of eleven isolated magnetic elements and an enhanced network region consisting of seventeen isolated magnetic elements. The conclusions are summarized in the following: At first, the magnetic elements of network and plage are intrinsically strong, and most of them (forty-one of forty-seven) are stronger than 970G. Secondly, we estimate that the intrinsic magnetic field strengths of quiet network are 689G to 1499G (fifteen of nineteen elements are stronger than 970G), those of plage are 1343G to 1960G, and those of enhanced network are 741G to 1976G (fifteen of seventeen elements are stronger than 1000G). Accordingly, we conclude that the intrinsic magnetic properties of different solar regions might be different, and one can not describe small-scale magnetic structures of different solar regions with the same model. At last, we find that there does not exist clear correlation between intrinsic field strength and magnetic filling factor.

The "strong field" view advises that most of magnetic flux in solar photosphere outside sunspots and pores is in forms of strong small scale magnetic structures. Our results confirm that this view is valid at least for the magnetic elements of plage and enhanced network. On the other hand, we must note that the intrinsic magnetic strengths trend to decrease from plage and enhanced network to quiet network, just as their apparent strengths do. This seems to imply that there exist some differences between the intrinsic

properties of network and plage, and we can not describe them with the same model. The apparent field strengths of intranetwork are much weaker than those of network. Are their intrinsic field strengths strong or weak? Unfortunately, we didn't detect this structure because the sensitivity of magnetic field measurement is not high enough in our observational mode. Some previous results had proven that intranetwork is weaker than network (Keller *et al.*, 1994; Wang *et al.*, 1995; *etc.*). If this is right, why does the field strength trend to decrease from plage, enhanced network, quiet network to intranetwork? What are the physical explanations? Further research must be expected.

Several authors had studied the correlation between filling factor and magnetic field strength (Tarbell and Title, 1977; Stenflo and Harvey, 1985; Zayer *et al.*, 1990). It is natural that the larger the filling factor is, the larger the apparent field strength is, just as what we have shown in Fig.5(b). About the intrinsic field strength, Stenflo and Harvey (1985) found that it varies from 800G to 1100G when the filling factor increases by a factor of 6. This weak correlation was also found by Tarbell and Title (1977) and Zayer *et al.* (1990). However, our result is not coincident with it. It is very difficult to explain this disagreement due to the following reasons: Firstly, the previous results were obtained by spectrometer system, while ours was obtained by filter system; Secondly, spatial resolution and sensitivity of magnetic field observation might be different for different authors; At last, different calibration methods might cause different results. Thus, farther observation and research are needed in order to obtain more knowledge about the correlation between intrinsic field strength and filling factor.

Acknowledgments

We thank Dr. Wang Jingshan, Dr. Song Guofeng, Dr. Wang Tongjiang, Dr. Zhang Hongqi, Dr. Wang Huaning and Dr. Liu Yang for their helps and discussions. We also thank Prof. Livingston for providing the spectral profiles. This program is supported by the Chinese Academy of Sciences and the National Natural Science Foundation.

References

Ai, G. X. and Hu, Y. F., 1987a, *Science in China*, P.868

Ai, G. X. and Hu, Y. F., 1987a, *Science in China,* P.1969

Ai, G. X. and Hu, Y. F., 1987c, *Acta Astrophysica Sinica*, 7, 305

Bernasconi P. N., Keller C. U., and Stenflo J. O., 1995, appear in: Balasubramaniam and Simon (*eds.*), *Proc. of the Fourteenth Sac. Peak Summer Workshop, Solar Active Region Evolution.*

Deng, Y. Y., Ai, G. X. and Wang, J. S., *et al.*, 1995, submitted to *Solar Phys.*.

Bruls, J. H. M. J., Solanki, S. K., 1995, *A&A.*, **293**, 240

Frazier, E. N. and Stenflo, J. O., 1972, *Solar Phys.*, **27**, 330

Frazier, E. N. and Stenflo, J. O., 1978, *A&A.*, **70**, 789

Howard, R., 1991, *Solar Phys.*, **134**, 233

Howard, R. and Stenflo, J. O., 1972, *Solar Phys.*, **22**, 402

Keller, C. U., Deubner, F. L., Egger, U., Fleck, B., Povel, H. P., 1994, *A&A.*, **286**, 626

Keller, C. U., Solanki, S. K., *et al.*, 1990, *A&A.*, **236**, 250

Lites, B. W. and Skumanich, A., 1990, *Ap.J.*, **348**, 747

Martin, S. F., 1988, *Solar Phys.*, **117**, 243

Rabin, D., 1992, *Ap. J.*, **390**, L103

Ruedi, I., Solanki, S. K., Livingston, W., Stenflo, J. O, 1992, *A&A.*, **263**, 323

Sanchez, J., Solanki, S. K., *et al.*, 1988, *A&A.*, **196**, 266

Sanchez, J. and Pillet, V., 1994, *Ap.J.*, **424**, 1014

Solanki, S. K., 1993, *space science reviews*, **63**, 1

Solanki, S. K., Keller, C. U. and Stenflo, J. O., 1987, *A&A.*, **188**, 183

Stenflo, J. O., 1973, *Solar Phys.*, **32**, 41

Stenflo, J. O. and Harvey, 1985, *Solar Phys.*, **95**, 99

Tarbell, D. and Title, A. M., 1977, *Solar Phys.*, **52**, 13

Wang, J. X., Wang, H. M., Tang, F., *et al.*, 1995, *Solar Phys.*, **160**, 277

Wiehr, E., 1978, *A&A.*, **69**, 279

Zayer, I., Solanki, S. K., et al., 1990, *A&A.*, **239**, 356

Zirin, H., 1987, *Solar Phys.*, **110**, 101

Captions

Figure 1: The Basic Structure Of Nine-Channel Solar Telescope

(a). Optical sketch of Nine-Channel Solar Telescope

(b). The universal birefringent filter used in NCST

UBF: universal birefringent filter; **PB**: polarizing beam splitter; **AR**: total reflective prism

The nine wavelengths designed in NCST are labeled at the right of (b)

a **PB** can split one incident beam into two emergent beams by their polarizing directions. Thus, one can obtain 2, 4, 8, 16, ··· beams simultaneously by using 1, 3, 7, 15 ··· PBs.

Figure 2. Longitudinal Magnetograms of FeI5250.22 Of Different Solar Regions

(a). Quiet network; **(b)**. Plage; **(c)**. Enhanced network

In each magnetogram, the field of view is 3.'7×2.'4 and the levels of field strength are 26, 52, 104, 156, 208, 312, 416, 800G, respectively. In the text, we analyze twenty-one quiet network magnetic elements, nineteen enhanced network elements and eleven plage elements. All of them are numbered.

Figure 3. Diagrams Of Magnetic Line Ratio *vs.* Apparent Field Strength

(a). Quiet network; **(b)**. Plage; **(c)**. Enhanced network

R: observed magnetic line ratio; **B**: apparent magnetic field strength

The number at upper right of each panel is the number of the analyzed magnetic element (See Fig. 2). One can see that the values of magnetic line ratio are compatible with a unique value in any magnetic element. Thus, there exists unique magnetic field. Note that the magnetic element No.08 of plage actually consists of three small elements, so there exist three 'unique' values in the left panel of (b).

Figure 4. The Calculated Calibration Curve

Solid line and **dash line** are obtained when the filter's passband is placed at -0.06 , and -0.075Åfrom the line center, respectively. **Dot line** is obtained when stray light is considered at -0.06Å from the line center. One can see that the calibration curve is sensible to the position of filter's passband, but not sensible to stray light.

Figure 5. The Dependence Of Filling Factor Upon Field Strength

(a). The curve of filling factor vs. intrinsic field strength

(b). The curve of filling factor vs. apparent field strength

Solid line: quiet network; **Dash line**: enhanced network; **Dot line**: plage

One can find that no clear correlation exists between intrinsic field strength and magnetic filling factor.

Table 1. Intrinsic Field Strengths And Filling Factors Of The Magnetic Elements Marked In Fig.2

(a). Quiet network; **(b)**. Plage; **(c)**. Enhanced network

No.: the number of each analyzed magnetic element (see Fig. 2);

R: observed magnetic line ratio; **ΔR**: r.m.s estimation of R;

B_I: intrinsic field strength; α: magnetic filling factor

One can see that fifteen of nineteen quiet network elements are stronger than 970G, fifteen of seventeen enhanced network elements are stronger than 1000G and all plage elements are stronger than 1300G. Note that B_I and α of No.20 and 21 of quiet network element can not be determined (see text).

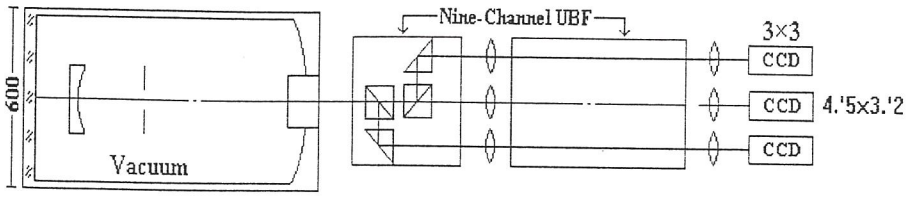

(a). Optical Sketch Of Nine-Channel Solar Telescope

UBF: universal birefringent filter

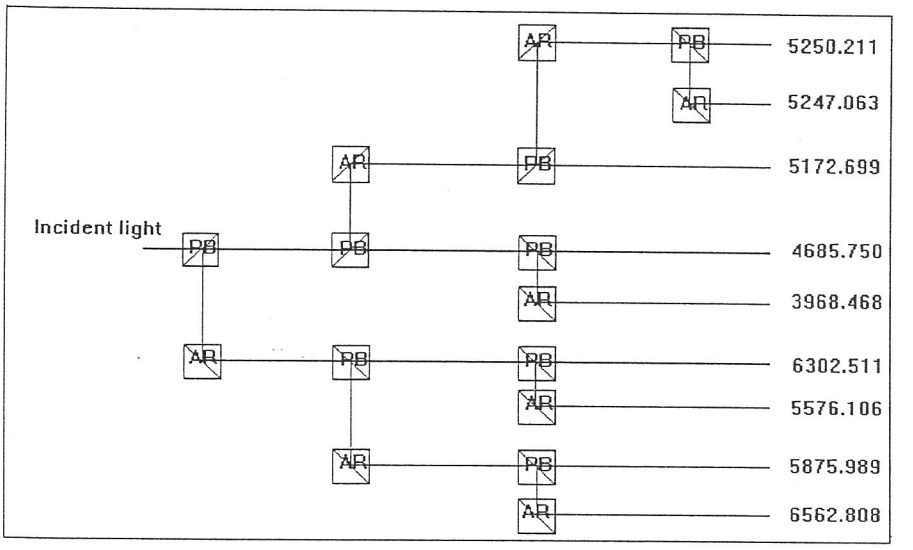

(b). The Universal Birefringent Filter Used In NCST

PB: polarizing beam splitter

AR: total reflective prism

Fig.1 The Basic Structure Of Nine-Channel Solar Telescope

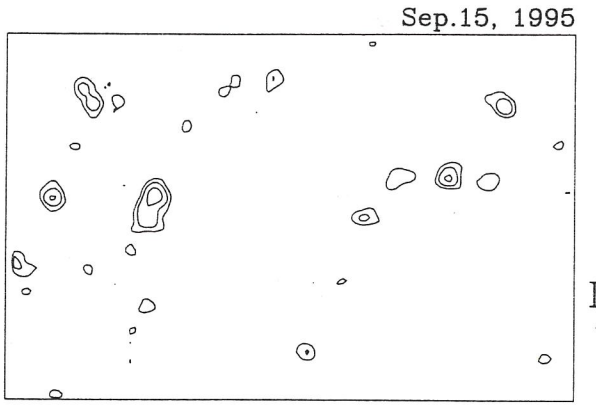

(a). quiet network

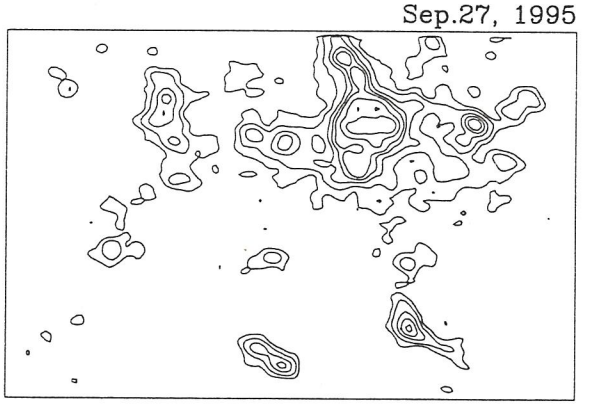

(b). plage region

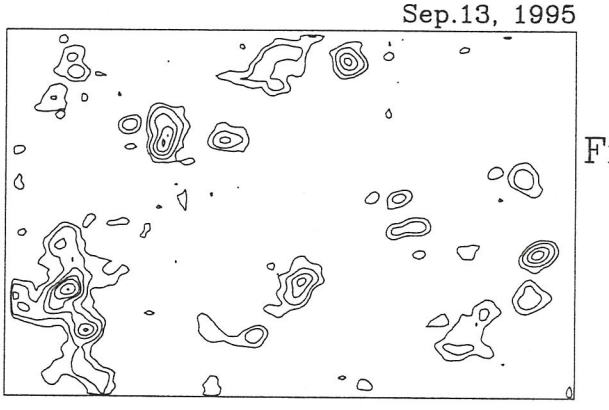

(c). enhanced network

Level: Gauss

26
52
104
156
208
312
416
800

Field of View

3.7*2.4

Fig.2 Longitudinal Magnetograms of FeI5250.22

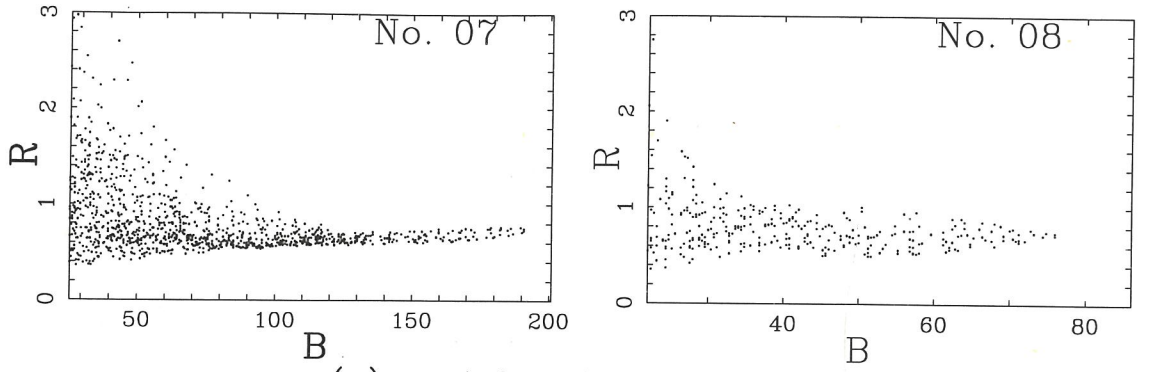

(a). quiet network

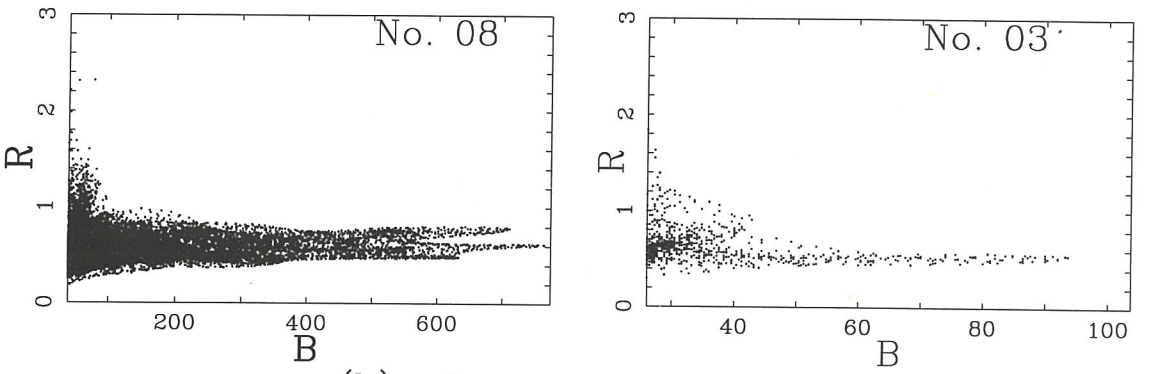

(b). plage

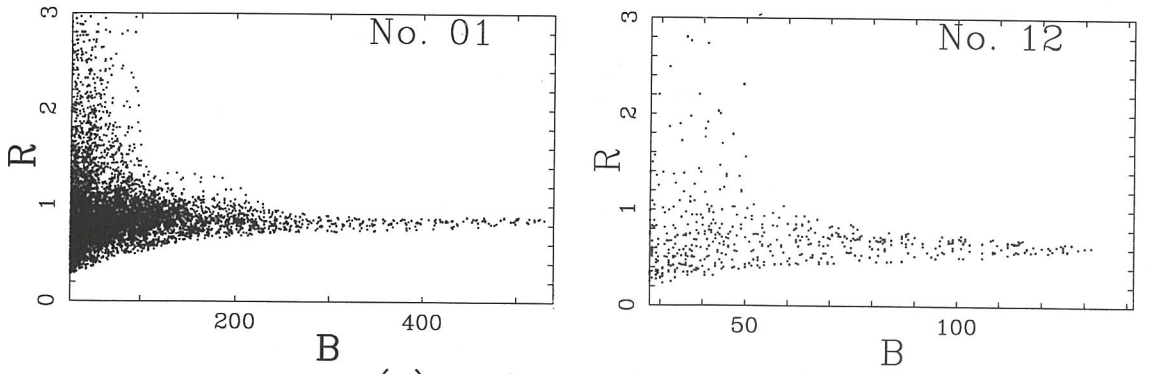

(c). enhanced network

Fig.3 Diagrams of Line Ratio vs. Apparent Field Strength

R: observed magnetic line ratio

B: apparent magnetic strength (in Gauss)

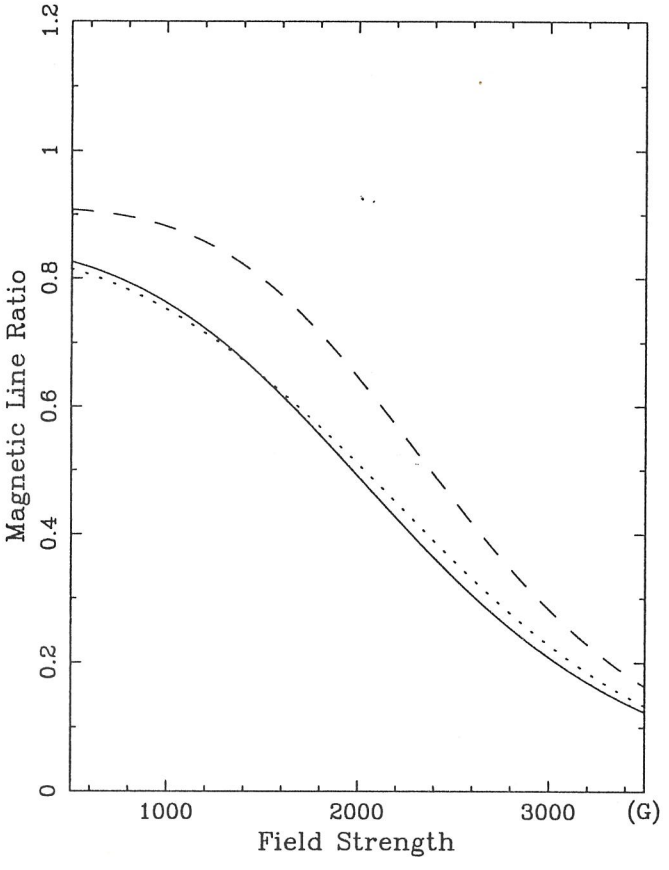

Fig.4 Calculated Calibration Curve

Solid line: passband of filter is at −0.06Å
Dash line: passband of filter is at −0.075Å
Dot line : passband of filter is at −0.06Å and stray light is considered (see text)

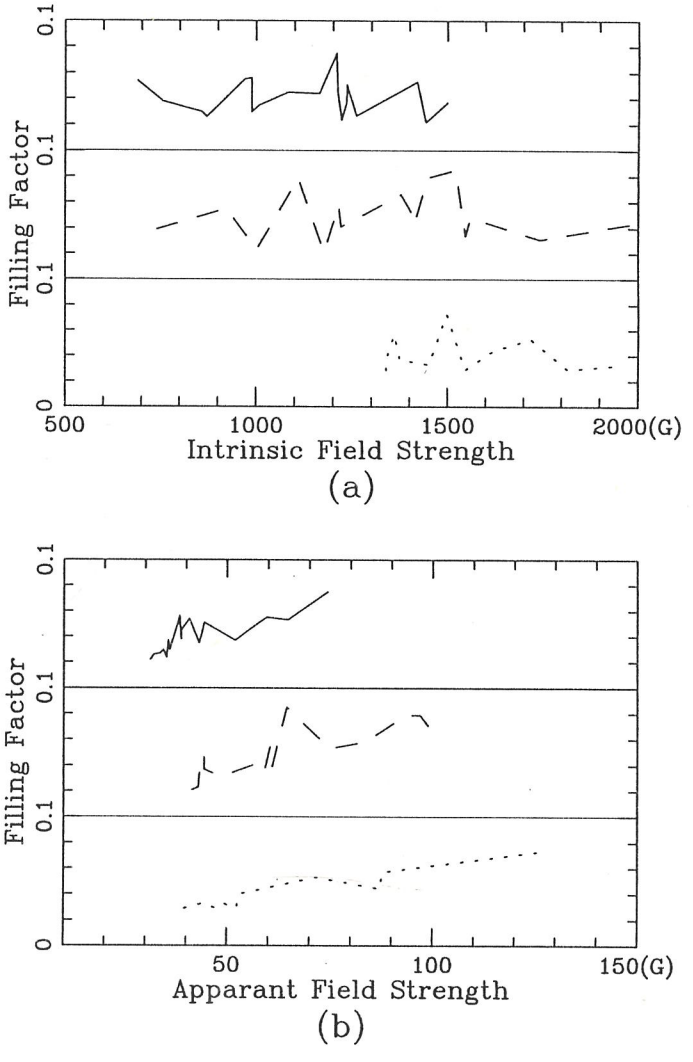

Fig.5 Dependence of Filling Factor Upon Field Strength

No.	1	2	3	4	5	6	7	8	9	10	11	12	13	14	15	16	17	18	19	20	21
R	.6617	.7837	.7078	.7854	.7160	.6459	.7631	.7630	.7992	.7189	.8085	.7604	.7463	.7131	.7135	.7290	.7675	.6679	.7190	.9315	1.072
ΔR	.1853	.1687	.1332	.1879	.1879	.2022	.2287	.1868	.2123	.2043	.2163	.1572	.2196	.1995	.2463	.1275	.2194	.1840	.2169	.1682	.1633
B_I	1443.	871.	1261.	858.	1222.	1499.	988.	988.	756.	1212.	689.	1008.	1083.	1236.	1235.	1164.	970.	1420.	1209.	-----	-----
α	.022	.051	.027	.045	.026	.024	.075	.045	.054	.053	.056	.038	.055	.044	.035	.030	.037	.037	.030	-----	-----

a. Quiet network

No.	1	2	3	4	5	6	7	8	9	10	11
R	.6320	.5037	.5495	.6598	.6881	.6798	.6872	.5808	.6117	.6835	.6464
ΔR	.1510	.1511	.0986	.1185	.2025	.2178	.1823	.1500	.1354	.2068	.1309
B_I	1547.	1960.	1818.	1452.	1339.	1375.	1343.	1720.	1621.	1361.	1499.
α	.057	.044	.029	.037	.040	.029	.053	.073	.029	.033	.033

b. Plage region

No.	1	2	3	4	5	6	7	8	9	10	11	12	13	14	15	16	17
R	.8605	.8818	.8186	.7845	.6951	.7326	.6703	.7884	.8885	.6540	.9005	.7939	.8209	.8542	.8690	.8116	.8254
ΔR	.2008	.1958	.1986	.2148	.2561	.2081	.1466	.2132	.2591	.1659	.1963	.2086	.2305	.2027	.2308	.1963	.2416
B_I	1177.	1001.	1413.	1560.	1859.	1742.	1221	1547.	923.	1976.	741.	1521	1404	1214.	1109.	1448.	1378.
α	.079	.043	.053	.031	.023	.034	.079	.039	.048	.021	.085	.066	.043	.037	.055	.058	.041

c. Enhanced network

Table 1. Intrinsic Field Strengths And Filling Factors Of The Magnetic Elements Marked In Fig.2

No.: the number of each analyzed magnetic element (see Fig. 2)

R: the observed magnetic line ratio ΔR: the r.m.s estimation of R

B_I: the intrinsic field strength α: the magnetic filling factor